

Studying the Physical Diversity of Late-M Dwarfs with Dynamical Masses^{*,†,‡}

Trent J. Dupuy,¹ Michael C. Liu,¹ Brendan P. Bowler,¹ Michael C. Cushing,²
Christiane Helling,³ Soeren Witte,⁴ and Peter Hauschildt⁴

ABSTRACT

We present a systematic study of the physical properties of late-M dwarfs based on high-quality dynamical mass measurements and near-infrared (NIR) spectroscopy. We use astrometry from Keck natural and laser guide star adaptive optics imaging to determine orbits for the late-M binaries LP 349-25AB (M7.5+M8), LHS 1901AB (M6.5+M6.5), and Gl 569Bab (M8.5+M9). We find that LP 349-25AB ($M_{\text{tot}} = 0.120_{-0.007}^{+0.008} M_{\odot}$) is a pair of young brown dwarfs for which Lyon and Tucson evolutionary models jointly predict an age of 140 ± 30 Myr, consistent with the age of the Pleiades. However, at least the primary component seems to defy the empirical Pleiades lithium depletion boundary, implying that the system is in fact older (if the parallax is correct) and that evolutionary models underpredict the component luminosities for this magnetically active binary. We find that LHS 1901AB is a pair of very low-mass stars ($M_{\text{tot}} = 0.194_{-0.021}^{+0.025} M_{\odot}$) with evolutionary model-derived ages consistent with the old age (> 6 Gyr) implied by its lack of activity. Our improved orbit for Gl 569Bab results in a higher mass for this binary ($M_{\text{tot}} = 0.140_{-0.008}^{+0.009} M_{\odot}$) compared to previous work ($0.125 \pm 0.007 M_{\odot}$ Simon et al. 2006). We use these mass measurements along with our published results for 2MASS J2206–2047AB (M8+M8) to test four sets of ultracool model atmospheres currently in use. Fitting these models to our NIR integrated-light spectra provides temperature estimates warmer by ≈ 250 K than those derived independently from Dusty evolutionary models given the measured masses and luminosities.

*Some of the data presented herein were obtained at the W. M. Keck Observatory, which is operated as a scientific partnership among the California Institute of Technology, the University of California, and the National Aeronautics and Space Administration. The Observatory was made possible by the generous financial support of the W. M. Keck Foundation.

†Based partly on observations obtained at the Canada-France-Hawaii Telescope (CFHT) which is operated by the National Research Council of Canada, the Institut National des Sciences de l'Univers of the Centre National de la Recherche Scientifique of France, and the University of Hawaii.

‡Based partly on observations made with ESO Telescopes at the Paranal Observatory under program IDs 073.C-0155, 077.C-0783, and 077.C-0441.

¹Institute for Astronomy, University of Hawai'i, 2680 Woodlawn Drive, Honolulu, HI 96822

²NASA Jet Propulsion Laboratory, 4800 Oak Grove Drive, Mail Stop 264-723, Pasadena, CA 91109

³SUPA, School of Physics and Astronomy, University of St. Andrews, North Haugh, St. Andrews KY16 9SS, UK

⁴Hamburger Sternwarte, Gojenbergsweg 112, 21029 Hamburg, Germany

We propose that model atmospheres are more likely to be the source of this discrepancy, as it would be difficult to explain a uniform temperature offset over such a wide range of masses, ages, and activity levels in the context of evolutionary models. This contrasts with the conclusion of Konopacky et al. (2010) that model-predicted masses (given input T_{eff} and L_{bol}) are at fault for differences between theory and observations. In addition, we find an opposite (and smaller) mass discrepancy from what they report when we adopt their model-testing approach: masses are too high rather than too low because our T_{eff} estimates derived from fitting NIR spectra are ≈ 650 K higher than their values from fitting broadband photometry alone.

Subject headings: binaries: close — binaries: general — binaries: visual — infrared: stars — stars: low-mass, brown dwarfs — techniques: high angular resolution

1. Introduction

While the spectra of late-M dwarfs are by definition very similar, their underlying nature can vary widely from youthful brown dwarfs to old low-mass stars. The first field dwarf with a spectral type later than M6 was discovered by van Biesbroeck (1944), yet even 50 years later the nature of such objects was open to debate, with Kirkpatrick et al. (1994) suggesting that the latest type M dwarfs may all be young enough to be substellar. Rebolo et al. (1992) proposed a method for discriminating between brown dwarfs and low-mass stars by using the Li I doublet at 6708 \AA , as models predict that stars and the highest mass brown dwarfs ($M \gtrsim 0.06 M_{\odot}$) should deplete their initial lithium rapidly. Such model predictions of lithium depletion have also been used to age-date open clusters (e.g., Stauffer et al. 1998; Barrado y Navascués et al. 1999). However, the underlying theory still remains unconstrained by direct mass measurements for ultracool dwarfs with lithium measurements near the predicted depletion boundary. In recent years, spectroscopic signatures of low surface gravity have been used to identify very young ($\sim 10\text{--}100$ Myr) ultracool dwarfs among the field population of late-M and L dwarfs (McGovern et al. 2004; Allers et al. 2007; Kirkpatrick et al. 2008; Rice et al. 2010), thus enabling a means of discriminating between stars and brown dwarfs if the objects are young enough.

Dynamical mass measurements provide a direct means for studying the diversity in the physical properties of late-M dwarfs. We present here masses for the late-M binaries LP 349-25AB, LHS 1901AB, and Gl 569Bab based on Keck natural guide star (NGS) and laser guide star (LGS) adaptive optics (AO) imaging from our ongoing orbital monitoring program targeting ultracool binaries. We combine our new measurements with published results to perform a systematic study of late-M dwarfs. To that end, we also present medium-resolution ($R \approx 2000$) near-infrared (NIR) spectra for this sample of late-M binaries. The resulting combination of high-quality dynamical masses and spectra enables strong tests of model atmospheres over a wide range of masses, ages, and activity levels.

LP 349-25 was first identified as a nearby M8 dwarf by Gizis et al. (2000), and Forveille et al. (2005) discovered its binary nature after being initially unresolved by Close et al. (2003). Gatewood & Coban (2009) measured a trigonometric parallax of 75.8 ± 1.6 mas for LP 349-25, corresponding to a distance of 13.2 ± 0.3 pc, which is somewhat more distant than the photometric estimate of 10.1 ± 1.2 pc (Forveille et al. 2005). Reiners & Basri (2009) obtained high-resolution integrated-light spectroscopy using Keck/HIRES and found no evidence for lithium (equivalent width $\lesssim 0.5$ Å). Konopacky et al. (2010) recently published a dynamical mass of $0.122 \pm 0.009 M_{\odot}$ based on Keck LGS AO data. We derive here a dynamical mass of $0.120_{-0.007}^{+0.008} M_{\odot}$, based on an independent set of astrometry. Thus, this binary is a pair of brown dwarfs.

LHS 1901 was first identified as a nearby M6.5 dwarf by Reid et al. (2003), and Lépine et al. (2009) have independently classified it as M7.0. Montagnier et al. (2006) discovered LHS 1901 to be a $0''.2$ binary, which was also later identified by Law et al. (2008). Lépine et al. (2009) measured the parallax of LHS 1901 to be 77.8 ± 3.0 mas, corresponding to a distance of 12.9 ± 0.5 pc. Our dynamical mass of $0.194_{-0.021}^{+0.025} M_{\odot}$ indicates that this is a pair of very low-mass stars in a highly eccentric orbit ($e = 0.830 \pm 0.005$).

Gl 569B was discovered as a companion to the chromospherically active M2 star Gl 569 by Forrest et al. (1988), and Martín et al. (2000) resolved it as an M8.5+M9 binary using Keck AO. There are three published orbit determinations for this binary (Zapatero Osorio et al. 2004; Simon et al. 2006; Konopacky et al. 2010) that all give consistent values of the total mass ($0.125 \pm 0.007 M_{\odot}$). However, these orbits are all based largely on astrometry from 1999 to 2001 obtained with the Keck NIR cameras KCAM and SCAM (the slit-viewing camera for NIRSPEC). Since these instruments are not astrometrically well-calibrated, we have derived a new orbit for Gl 569Bab based solely on data from Keck/NIRC2 and the *Hubble Space Telescope* (*HST*) Space Telescope Imaging Spectrograph (STIS). In addition, we use the revised *Hipparcos* parallax for Gl 569A of 103.59 ± 1.72 mas (van Leeuwen 2007) rather than the original value of 101.91 ± 1.67 mas (Perryman & ESA 1997) used in all previous orbit determinations. Our improved measurement of the total dynamical mass for Gl 569Bab is $0.140_{-0.008}^{+0.009} M_{\odot}$, indicating that the binary is more massive than previously thought but still with at least one unambiguously substellar component.

In addition to these three binaries, we include the M8+M8 binary 2MASS J22062280–2047058AB (hereinafter 2MASS J2206–2047AB) in our study as it also has a well-determined mass ($0.15_{-0.03}^{+0.05} M_{\odot}$; Dupuy et al. 2009a) and integrated-light spectroscopy.¹

¹The only other late-M dwarf binary with a precise dynamical mass is LHS 1070BC ($M_{\text{tot}} = 0.157 \pm 0.009 M_{\odot}$ Leinert et al. 2001; Seifahrt et al. 2008), but it is only $1''.5$ from the bright primary LHS 1070A (M5.5) making it difficult to obtain spectroscopy of the late-M dwarfs. We also do not consider four other late-M dwarf binaries from Konopacky et al. (2010), as their dynamical masses are poorly constrained with 60–190% errors.

2. Observations

2.1. Keck/NIRC2 AO

We have monitored LP 349-25AB, LHS 1901AB, and Gl 569Bab with the AO system at the Keck II Telescope on Mauna Kea, Hawaii, using the facility NIR camera NIRC2 in its narrow field-of-view mode. At each epoch, we obtained data in one or more filters covering the standard atmospheric windows from the Mauna Kea Observatories (MKO) filter consortium (Simons & Tokunaga 2002; Tokunaga et al. 2002). For LP 349-25AB, we used LGS AO (Wizinowich et al. 2006; van Dam et al. 2006) when observing conditions allowed, and NGS AO otherwise (see Table 1). The LGS brightness, as measured by the flux incident on the AO wavefront sensor, was equivalent to a $V \approx 9.5$ – 10.4 mag star. The tip-tilt correction and quasi-static changes in the image of the LGS as seen by the wavefront sensor were measured contemporaneously by a second, lower bandwidth wavefront sensor monitoring LP 349-25, which saw the equivalent of an $R \approx 14.3$ – 14.6 mag star. For LHS 1901AB, we used NGS AO (Wizinowich et al. 2000; van Dam et al. 2004), and the incident flux on the wavefront sensor from LHS 1901 was equivalent to a $V \approx 13.0$ – 13.4 mag star. For Gl 569Bab, the primary star Gl 569A ($R = 9.4$ mag) located $5''0$ from the science target provided the NGS AO correction.

Our procedure for obtaining, reducing, and analyzing our images is described in detail in our previous work (e.g., Dupuy et al. 2009b,c). Table 1 summarizes our observations of LP 349-25AB, LHS 1901AB, and Gl 569Bab. The binary separation, position angle (PA), and flux ratio were determined using the same three-component Gaussian representation of the point-spread function (PSF) as described in Dupuy et al. (2009c). At epochs where the binary was sufficiently well-separated, we were also able to use the StarFinder software package (Diolaiti et al. 2000) to simultaneously solve for the PSF and binary parameters. As described in Dupuy et al. (2009c), we assessed systematic errors in both PSF-fitting procedures by applying them to artificial binary images constructed from images of PSF reference stars with similar FWHM and Strehl. We found good agreement between both methods, with StarFinder typically giving equivalent or smaller errors. We adopted the astrometric calibration of Ghez et al. (2008), with a pixel scale of 9.963 ± 0.005 mas pixel $^{-1}$ and an orientation for the detector’s $+y$ -axis of $+0^\circ 13 \pm 0^\circ 02$ east of north. We applied the distortion correction developed by B. Cameron (2007, private communication), which changed our astrometry below the 1σ level. The resulting relative astrometry and flux ratios for LP 349-25AB, LHS 1901AB, and Gl 569Bab are given in Table 2.

For Gl 569Bab, we also used our Keck images to measure relative photometry between the primary star Gl 569A and Gl 569Bab at JHK , as there is no photometry published in the MKO system. We summed the flux in circular apertures with radii of $0''.3$ to $0''.5$. We used NIRC2 in subarray mode to reduce the minimum allowed exposure time and thus avoid saturating the primary, which limited the size of the largest aperture we could use. However, in experimenting with even smaller apertures we found the same relative photometry to within 1σ . We used a portion of the array minimally affected by light from either the bright primary star or the binary to measure the

median sky level, which was subtracted from our summed aperture fluxes. The relative flux of the binary in integrated light compared to Gl 569A was $\Delta J = 4.15 \pm 0.05$ mag, $\Delta H = 4.14 \pm 0.03$ mag, and $\Delta K = 3.86 \pm 0.03$ mag. To compute absolute photometry for Gl 569B we applied these flux ratios to MKO photometry for Gl 569A, which was derived by converting its Two Micron All Sky Survey (2MASS) photometry to the MKO system using offsets computed from synthetic photometry of a SpeX prism spectrum of Gl 569A (A. Burgasser 2010, private communication). The conversions from 2MASS to MKO for J , H , and K were -0.03 mag, $+0.02$ mag, and -0.01 mag, respectively (all $\leq 1.3\sigma$ compared to the 2MASS errors). Thus, the final MKO integrated-light photometry for Gl 569B was $J = 10.75 \pm 0.06$ mag, $H = 10.15 \pm 0.04$ mag, $K = 9.62 \pm 0.03$ mag.

2.2. *HST*/STIS Imaging

Gl 569Bab was observed by *HST*/STIS on 2002 June 26 UT as part of a program to obtain resolved optical spectroscopy of ultracool binaries (GO-9499; PI Martín). During acquisition, the STIS CCD imager took two images with the long-pass filter F28X50LP in which the binary is well-detected and the primary star Gl 569A is saturated.² We analyzed these images using our PSF-fitting routine based on the TinyTim model of the *HST* PSF (Krist 1995), as described in our previous work (e.g., Liu et al. 2008; Dupuy et al. 2009a). We adopted the pixel scale and distortion solution from the STIS Instrument Science Report 2001-02 (Walsh et al. 2001, 50.725 ± 0.056 mas pixel⁻¹).

We tested for systematic errors in our best-fit binary parameters by applying our PSF-fitting routine to artificial binary images created from STIS CCD images of single stars from *HST* calibration programs in Cycles 8 and 10 (CAL/STIS-8422 and 8924). To preserve the undersampled nature of the PSF, we created only artificial binaries separated by an integer number of pixels. The separation and instrumental PA of Gl 569Bab in the STIS images were 1.92 pixels and $3^\circ 1$, so artificial binaries with $\Delta(x, y) = (0, 2)$ were an excellent representation of the science data. The single stars were $\approx 10\times$ brighter in the STIS images than Gl 569Ba, so we scaled them to match the science data and then injected them into the actual science image to accurately simulate the noise. The binary images were injected at a distance of $5''$ from Gl 569A, chosen to be comparable to Gl 569B’s separation. For the final adopted errors we used the larger of the rms from the artificial binaries or the rms of the best-fit parameters to the science data. From our artificial binary tests, we found systematic offsets in separation (3.0 mas, 2.3σ), PA ($0^\circ 2$, 0.2σ) and flux ratio (0.15 mag, 5σ), which we applied to our best-fit binary parameters for Gl 569Bab. The final separation, PA, and flux ratio we derived were 97.3 ± 1.3 mas, $94^\circ 0 \pm 0^\circ 9$, and 0.99 ± 0.03 mag (Table 2).

²F28X50LP has a cut-on wavelength around $0.55 \mu\text{m}$ and extends as red as $1.0 \mu\text{m}$.

2.3. VLT/NACO

We retrieved archival images of LP 349-25AB obtained with the Very Large Telescope (VLT) at Paranal Observatory on five epochs spanning six months in 2006. These data were taken with the NACO adaptive optics system (Lenzen et al. 2003; Rousset et al. 2003) using the N90C10 dichroic and S13 camera. We adopt the pixel scale of 13.221 ± 0.017 mas pixel⁻¹ derived by B. Sicardy (2008, private communication)³ from observations of Pluto’s motion compared to its known ephemeris, and an orientation of the detector of $0^\circ 0' \pm 0^\circ 1'$ (Forveille et al. 2005). We followed the same procedure for analyzing these data as in our previous work with VLT images (Dupuy et al. 2009a,c). We registered, sky-subtracted, and performed cosmic ray rejection on the raw archival images. We used the same analytic PSF-fitting routine as was used for the Keck data to fit the VLT images, with uncertainties determined from the standard deviation of measurements from individual dithers. The resulting best-fit parameters are summarized in Table 2.

2.4. Previously Published Astrometry

Forveille et al. (2005) published two epochs of astrometry for LP 349-25AB, and we investigated the possibility of improving the precision of their measurements by applying our PSF-fitting procedure to their data, which is in public archives. The CFHT observations of LP 349-25AB on 2004 July 3 UT were not available in the CFHT archive because they were obtained during engineering time (T. Forveille 2010, private communication), but the VLT/NACO observations from 2004 September 24 UT are in the VLT archive. We measured a separation of 111.2 ± 0.3 mas, a PA of $5.66 \pm 0.12^\circ$, and a flux ratio at H band of 0.40 ± 0.03 mag. Our flux ratio and separation are in good agreement with those measured by Forveille et al. (2005), 0.38 ± 0.05 mag and 107 ± 10 mas, while our PA of $5.66 \pm 0.12^\circ$ is somewhat inconsistent with their $7.1 \pm 0.5^\circ$ (at 2.8σ). We tried using each of these measurements to fit the orbit and found that they gave consistent dynamical masses with a very similar χ^2 for the best-fit. Our higher precision measurement would enable the uncertainty in some of the orbital parameters to be improved by up to a factor of ≈ 2 . However, we conservatively chose to use the published astrometry of Forveille et al. (2005) as their larger errors and PA offset may result from analysis of astrometric calibration data unavailable to us that was taken along with their observations.

Montagnier et al. (2006) published three epochs of astrometry for LHS 1901AB, and the first two data sets are available in the CFHT archive. Unfortunately, not all of the astrometric calibration data was available in the archive, so independent measurements from these data cannot be used in the orbit fit because, e.g., the orientation of the detector at the time of those observations is not accurately known. Montagnier et al. (2006) found uncertainties of 5 mas and 0.5° for all three data sets. The rms scatter of our PSF-fitting measurements is comparable or slightly lower (3–4 mas

³http://www.eso.org/sci/facilities/paranal/instruments/naco/doc/VLT-MAN-ESO-14200-2761_v83.3.pdf

and $0.4\text{--}0.6^\circ$), and thus even with the needed calibration data a drastic improvement in precision seems unlikely. Thus, we use the published astrometry of Montagnier et al. (2006) when fitting the orbit of LHS 1901AB (Table 2).

For Gl 569Bab, we do not use any of the previously published astrometry. We performed our own analysis on the original Keck/NIRC2 images from Simon et al. (2006) following the method described in Section 2.1. Konopacky et al. (2010) published one epoch of astrometry for Gl 569Bab which is contemporaneous with our 2009 May data; we conservatively choose to exclude their data from our orbit fit, although it is consistent with our best-fit orbit. We do not include any of the Keck/KCAM or SCAM astrometry published by Lane et al. (2001) or Zapatero Osorio et al. (2004), as those cameras have not been rigorously astrometrically calibrated, unlike NIRC2 and the STIS CCD.

2.5. IRTF/SpeX Spectroscopy

In addition to astrometry, which we use to determine orbits and thus dynamical masses, we have also obtained NIR spectra to perform tests of model atmospheres, as discussed in Sections 3 and 4. Using the NASA Infrared Telescope Facility (IRTF) spectrograph SpeX (Rayner et al. 2003), we obtained spectra of LP 349-25, LHS 1901, and Gl 569B on 2008 July 6, 2010 January 30, and 2010 March 3 UT, respectively. We used SpeX in cross-dispersed (SXD) mode, with five orders spanning $0.81\text{--}2.42\ \mu\text{m}$. For LP 349-25 we used a $0''.5$ slit ($R = 1200$), and for LHS 1901 and Gl 569B we used a $0''.3$ slit ($R = 2000$). We calibrated, extracted, and telluric-corrected the data using the SpeXtool software package (Vacca et al. 2003; Cushing et al. 2004). We used integrated-light photometry from 2MASS to flux-calibrate our spectra of LP 349-25 and LHS 1901. For Gl 569B, we used our own integrated-light photometry derived from our Keck images (Section 2.1) to flux calibrate its spectrum. We used the mean of the *JHK* scaling factors computed for each bandpass to place our spectra on an absolute flux scale.

3. Results

3.1. Orbit Determination and Dynamical Masses

Combining our Keck AO monitoring with published discovery data, we have observations spanning 5.9 years for LP 349-25AB, 5.9 years for LHS 1901AB, and 7.9 years for Gl 569Bab. Following our previous studies, we have determined the orbital parameters and their uncertainties using both a Markov Chain Monte Carlo (MCMC) approach, described in detail by Liu et al. (2008), as well as the least-squares minimization routine ORBIT (Forveille et al. 1999). In addition, we have developed our own visual binary orbit fitting routine that utilizes the Levenberg-Marquardt algorithm as implemented in the MPFIT routine for IDL (Markwardt 2009). To determine uncertainties on

the best-fit parameters from this routine, we have performed Monte Carlo simulations in which Gaussian noise is added to the data corresponding to their measurement uncertainties. We used the resulting distributions to determine the medians and standard deviations of the best-fit parameters. When multiple astrometric measurements were available from different bandpasses at a single epoch, we used the highest precision measurement in the orbit fit (see Table 2). The best-fit orbits are shown in Figures 1 and 2.

We found essentially symmetric uncertainties in the MCMC-derived orbital parameters for LP 349-25AB. These parameters agreed to within $< 0.5\%$ of those derived by our custom fitting routine, and the errors agreed to within $< 15\%$. As an additional test of our Levenberg-Marquardt fitting routine, we found that the best-fit parameters from `ORBIT` also agreed to within $< 1\%$, and the errors derived from our Monte Carlo approach agreed to within $< 10\%$ of the errors computed from the full covariance matrix in `ORBIT`. The orbital parameters and errors derived by our MCMC analysis and custom fitting routine are given in Table 3.

We experimented with including the five epochs of relative astrometry from Konopacky et al. (2010) when fitting the orbit of LP 349-25AB. If all of their data are included, the χ^2 becomes unrealistically large: χ^2 of 58.2 for 31 degrees of freedom (DOF). This large χ^2 value is due to the fact that two of their measurements from 2007 December and 2008 May are extreme outliers from the best-fit orbit. (Indeed, their own orbit fit is inconsistent with these data as the Konopacky et al. 2010 orbit has a reduced χ^2 of 2.15, which is unrealistically large.) By excluding their most discrepant epoch (2008 May 30 UT), we were able to achieve a reasonable χ^2 (33.1 for 29 DOF). Neither the orbital parameters nor their uncertainties change significantly after including the Konopacky et al. (2010) data. This is because their astrometry does not offer additional unique constraints on the orbit, as it was obtained contemporaneously with ours and is of lower precision by a factor of ≈ 4 to 10. Thus, we conservatively choose to exclude the Konopacky et al. (2010) astrometry from our analysis. Our best-fit total mass (M_{tot}) for LP 349-25AB is $0.1205 \pm 0.0007 M_{\odot}$ (0.6%), and after including the 2.1% error in the parallax this becomes $0.120_{-0.007}^{+0.008} M_{\odot}$ (6%).

From our MCMC analysis of LHS 1901AB, we found significant asymmetries in the posterior probability density distributions of the orbital period, semimajor axis, and eccentricity. The confidence limits on all orbital parameters are given in Table 3, and the distributions of these three parameters are shown in Figure 3. The orbital period and semimajor axis display a high degree of covariance as expected (e.g., see Section 3.2 of Dupuy et al. 2009b). There appear to be two slightly degenerate solutions, with one having a shorter period, lower eccentricity, and higher mass than the other. Our MCMC analysis enables us to treat this degeneracy properly by accounting for it in the confidence limits of these orbital parameters and the resulting dynamical mass. The difference in mass between these two solutions is very small (about 1.6%), insignificant compared to the 12% error contributed by the distance uncertainty. Our best-fit total mass for LHS 1901AB is $0.1944 \pm 0.0028 M_{\odot}$ (1.4%), and after including the $_{-3.7}^{+4.0}\%$ error in the parallax this becomes $0.194_{-0.021}^{+0.025} M_{\odot}$ (12%).

The orbital parameters we find from Gl 569Bab are all consistent with previously published orbits, with a singular exception. The semimajor axis we find ($95.6_{-1.0}^{+1.1}$ mas) is 4.3σ higher than the value of 90.4 ± 0.7 mas derived by Simon et al. (2006), and the Zapatero Osorio et al. (2004) and Konopacky et al. (2010) values are similarly discrepant (by 1.6σ and 3.7σ , respectively). Since all orbit determinations to date have been dominated by the nine epochs of astrometry from Keck KCAM and SCAM, the semimajor axis discrepancy implies that the pixel scale of one or both of these instruments was underestimated by $\approx 5\%$, resulting in systematically low semimajor axes. This is supported by the fact that the previously published NIRC2 astrometry from Simon et al. (2006) and Konopacky et al. (2010) is in good agreement with our best-fit orbit. Also, the *HST*/STIS measurement would be highly inconsistent with a value for the semimajor axis as low as previously found, showing that our semimajor axis is not simply due to a problem with the NIRC2 calibration.⁴ Since we find the same orbital period as in previous work but a semimajor axis that is 5.4% larger, our dynamical total mass is significantly higher than previously found. This would be a 16% effect, but it is moderated somewhat by the revised *Hipparcos* parallax that is 1.6% (about 1σ) higher than the original value, which brings the mass down by 4.8% for a net change of 11%. Our best-fit total mass for Gl 569Bab is $0.140_{-0.004}^{+0.005} M_{\odot}$, and after accounting for the 1.6% parallax error this becomes $0.140_{-0.008}^{+0.009} M_{\odot}$. Our MCMC analysis also reveals a slightly degenerate orbit solution with double-peaked distributions for the argument of periastron (ω) and PA of the ascending node (Ω) as shown in Figure 3. The degeneracy in these values are apparently not correlated with any other orbital parameters.

3.2. Spectral Types

Gizis et al. (2000) used the integrated-light optical spectrum of LP 349-25 to derive a spectral type (SpT) of $M8.0 \pm 0.5$. Comparing our near-infrared spectrum of LP 349-25 to spectra of M dwarf standards from the IRTF Spectral Library (Cushing et al. 2005; Rayner et al. 2009), we find an infrared spectral type of M8. Without resolved spectroscopy of the binary, we cannot directly determine the spectral types of the individual components. However, we have used our photometry and the empirical SpT–absolute magnitude relations of Cruz et al. (2003, *J* band only) and Golimowski et al. (2004, *L'* band only) to estimate spectral types. We used the method described by Dupuy et al. (2009c), which accounts for both the measurement uncertainties and the intrinsic scatter in the empirical absolute magnitude relations. We found that the range of *J*-band absolute magnitudes allowed by our measurement errors exceeded the bounds of the Cruz et al. (2003) relation, and thus we base our estimates only on the *L'*-band relation. We estimate spectral types of $M7.5 \pm 1.0$ for the primary and $M8.0_{-1.0}^{+1.5}$ for the secondary, which are consistent with the published integrated-light spectral type.

⁴We also note that a calibration problem with NIRC2 would have been apparent in our previously published binary orbits, which typically have data from NIRC2 as well as other well-calibrated instruments such as *HST*/WFPC2-PC, *HST*/ACS-HRC, and VLT/NACO.

Reid et al. (2003) measured the integrated-light spectral type of LHS 1901 to be M6.5, and Lépine et al. (2009) measured M7.0. Our near-infrared spectrum is better matched by the M dwarf standard vB 8 (M7) than GJ 1111 (M6.5), thus we find an infrared type of M7 for LHS 1901. Using the method described above, the J -band absolute magnitudes of the individual components provide an estimated spectral type of $M6.5^{+1.0}_{-0.5}$ for both the primary and secondary, consistent with measured integrated-light spectral types. The difference of zero subtype between the components is also consistent with our measured flux ratios and late-M dwarfs with known parallaxes. For example, the rms scatter among K -band absolute magnitudes for M6.5 dwarfs is 0.12 mag (cf. $\Delta K = 0.107 \pm 0.007$ mag for LHS 1901AB).

For Gl 569Bab, we adopt the spectral types of $M8.5 \pm 0.5$ and $M9.0 \pm 0.5$ derived by Lane et al. (2001). They used their resolved near-infrared spectra of the individual components to compute spectral indices and compared these values to field dwarfs of known spectral type. They found a difference of 0.5 subtypes between the two components and assigned the integrated-light spectral type of M8.5 from Henry & Kirkpatrick (1990) to the primary, resulting in a type of M9.0 for the secondary. These spectral types are consistent with those found by Martín et al. (2006, M9+M9) using resolved optical spectroscopy of Gl 569Bab from *HST*/STIS.

3.3. Bolometric Luminosities

We computed the total bolometric luminosities (L_{bol}) of our sample binaries from their integrated-light spectra and photometry. In addition to our SpeX spectra, we used the L' and M' band photometry from Golimowski et al. (2004) and the $24 \mu\text{m}$ *Spitzer* photometry from Gautier et al. (2007) for LP 349-25, and we used the L' band photometry from Forrest et al. (1988) for Gl 569B. For LHS 1901, we estimated a $K - L'$ color of 0.56 ± 0.07 mag from the empirical relation of Dupuy et al. (2009a) to extend its SED to longer wavelengths. To accurately account for the SED at shorter wavelengths, we appended optical spectra, using the overlapping region of our SpeX spectra to determine the flux scaling. For LP 349-25 and Gl 569B we used optical spectra from Reid et al. (2003) and Henry & Kirkpatrick (1990), respectively. For LHS 1901 we used the optical spectrum of the M7 standard vB 8 (Henry & Kirkpatrick 1990). We numerically integrated the spectra and photometry points, interpolating between the gaps in the data, extrapolating to zero flux at zero wavelength, and assuming a Rayleigh-Jeans tail beyond the last photometric point. We accounted for errors as described in Dupuy et al. (2009a), finding a total $\log(L_{\text{bol}}/L_{\odot})$ of $-2.804^{+0.026}_{-0.019}$ dex for LP 349-25, $-2.67^{+0.04}_{-0.03}$ dex for LHS 1901, and -3.212 ± 0.018 dex for Gl 569B.

We apportioned these total bolometric fluxes to the individual components by using the measured K -band flux ratio and the bolometric correction–SpT relation derived by Golimowski et al. (2004), properly accounting for uncertainties in the component spectral type estimates. The resulting individual luminosities are given in Table 4. For the components of Gl 569Bab, our L_{bol} values are in good agreement with the estimates from Lane et al. (2001). As in our previous work, we correctly account for the covariance between the individual luminosities (via the flux ratio) in

the following analysis, allowing more precise determinations of relative quantities (e.g., ΔT_{eff} and the mass ratio).

3.4. T_{eff} and $\log(g)$ from Model Atmosphere Fitting

We used a variety of solar-metallicity model atmosphere grids to fit our integrated-light IRTF/SpeX spectra, summarized in Table 5. The two publicly available grids we used are Ames-Dusty (Allard et al. 2001) and PHOENIX-Gaia (Brott & Hauschildt 2005). We also used an improved version of Ames-Dusty that employs the same treatment of dust but with updated line lists for some important opacity sources such as FeH, CrH, and H₂O (see Section 3.2 of Rice et al. 2010); this “Gaia-Dusty” model grid is the same as that employed by Konopacky et al. (2010). Our fourth model grid Drift-PHOENIX (Witte et al. 2009) relies on yet another gas opacity data set and, more importantly, features improved dust opacities. The model treats the dynamics of the dust in a presently unrivaled level of detail by calculating the rate of seed formation and solving an actual growth rate equation system for gravitational settling of composite grains (Woitke & Helling 2003; Helling & Woitke 2006; Helling et al. 2008).

We fit model atmospheres to our spectra using the procedure outlined by Bowler et al. (2009). For every model spectrum, we found the optimal scaling factor to match the observed spectrum by minimizing the χ^2 statistic. The model spectrum with the lowest resulting χ^2 value gives the best-fit parameters for T_{eff} and $\log(g)$. For each spectrum, we fit individual wavelength ranges corresponding to the standard near-infrared bandpasses (*YJHK*). We also performed fits to the entire SED, both with and without the segment of the spectrum between 0.81 and 0.95 μm . This region of the spectrum is often excluded when fitting models to L and T dwarfs (e.g., Cushing et al. 2008) because it is strongly affected by the broad wings of the resonant K I doublet at 0.77 μm , which have long been difficult to model (e.g., Burrows & Volobuyev 2003) and can be impacted by dust modeling (Johnas et al. 2008). Such alkali lines are present but weaker in late-M dwarfs, and they may contribute to observed discrepancies with models between ≈ 0.7 and 0.9 μm for objects as early as L0 (Reiners et al. 2007).

The results of our model atmosphere fitting procedure are given in Table 6. We report fits both for our full wavelength range (0.81–2.42 μm) and for the NIR only (0.95–2.42 μm). We prefer the NIR SED fits for the following reasons: (1) the NIR SED fits are more consistent with the individual *YJHK* band fits (typically within one model grid step of 100 K, 0.5 dex in $\log(g)$); (2) the full SED fits are systematically cooler by ≈ 100 K compared to the individual band fits, implying that the lowest *S/N* portion of the spectrum from 0.81 to 0.95 μm has a disproportionate influence on the results; and (3) by adopting a 0.95 μm cutoff here, our results will be directly comparable to future work on L and T dwarfs that require such a cutoff because of the problems with K I lines.

Figure 4 shows the χ^2 contours of the fits to our observed NIR spectral energy distributions

(SEDs) using all model spectra. The elongation of the contours in the $\log(g)$ direction indicates that gravity is less well-constrained by our fits than effective temperature. We also note that there are occasionally local χ^2 minima in these plots that correspond to physically implausible parameters. For Drift-PHOENIX, the deviant χ^2 minimum occurs at very low temperatures (2000 K) and high gravities ($\log(g) = 6.0$, which for masses of $<0.08 M_\odot$ correspond to radii of $<0.045 R_\odot$, more than a factor of two lower than evolutionary model predicted radii). For the other three model grids, χ^2 minima extend to higher temperatures (≈ 3300 K) and extremely low gravities ($\log(g) = 3.5$, which for masses of $>0.06 M_\odot$ correspond to radii of $>0.7 R_\odot$). In the rare cases when the global minimum is found in one of these physically implausible regions ($\approx 3\%$ of fits, see Table 6), we select the second best fitting model instead, and this always results in best-fit parameters from the prevailing solutions of $T_{\text{eff}} = 2700\text{--}3000$ K.

The different grids of model atmospheres generally give very similar best-fit parameters despite their significantly different input assumptions. For example, the treatment of dust in the Drift-PHOENIX models is much more realistic than in other models, yet for our sample it yields the same T_{eff} values as other grids. Thus, it appears that the effects of dust at the warm temperatures of late-M dwarfs only subtly impact the resultant model spectra for our purposes. In fact, for the NIR SED fits (0.95–2.42 μm), all four sets of models give exactly the same T_{eff} .

Finally, we investigated how binarity impacts the atmospheric parameters derived from integrated-light spectra. We constructed artificial binary integrated-light spectra by summing individual IRTF/SpeX SXD spectra, both from our own spectra (e.g., summing the spectra of LP 349-25 and Gl 569B) and from publicly available spectra of the M7, M8, and M9 spectral standards vB 8, vB 10, and LHS 2924 (Cushing et al. 2005; Rayner et al. 2009). We fit these spectra both individually and summed, after scaling down the later type spectrum to best match the measured JHK flux ratios of LP 349-25AB and Gl 569Bab.⁵ Comparing the summed and input “primary” spectrum fits, we found that the best-fit values from individual bands were nearly identical (at most different by one grid step of 100 K or 0.5 dex). In some cases we found that the summed spectra gave systematically lower temperatures of 100 K as compared to the input “primary” spectrum. However, this was not the case when the input spectra had JHK colors comparable to the components of LP 349-25AB and Gl 569Bab. We note that within each binary the components have very similar JHK colors, so we might expect that simulated component and summed spectra would give the same results. For example, the integrated-light $J - K$ color of LP 349-25 is 1.02 mag, and its components are only different by ≈ 0.03 mag ($J - K = 1.00$ mag and 1.05 mag) despite the binary flux ratio of ≈ 0.3 mag (the $H - K$ and $J - H$ colors are even closer, $\Delta\text{color} \approx 0.01$ mag).

In summary, our simulations show that the individual band fits should be unaffected by con-

⁵LHS 1901 and 2MASS J2206–2047 both have flux ratios within ≈ 0.1 mag of unity across $JHKL'$ bandpasses and thus have components that are likely to be spectrally identical. For example, LHS 1901 has a bolometric flux ratio of 0.044 ± 0.015 dex, and thus the difference in T_{eff} between the individual components is expected to be 75 K (i.e., less than one model grid step) for an assumed radius ratio of unity.

tamination from the spectrum of the secondaries in our sample binaries, and even if the SED fits are affected they will give T_{eff} values systematically lower by only 100 K. Given that our best-fit values of the NIR SEDs show no such systematic offsets from the band fits, we conclude that our fits to the integrated-light spectra accurately find the best-fit parameters of the primary component’s spectrum.

3.5. Age Constraints from Kinematics and Activity

We have considered whether the space motion and activity of our sample binaries can provide useful constraints on their ages. For LP 349-25, there are two discrepant measurements of its radial velocity (RV) in the literature: (1) Reiners & Basri (2009) derived $-16.8 \pm 2.0 \text{ km s}^{-1}$ from cross-correlation of their Keck/HIRES spectrum with the RV standard Gl 406 (M6); and (2) Konopacky et al. (2010) found a center-of-mass velocity of $-8.0 \pm 0.5 \text{ km s}^{-1}$ by fitting an orbit to their multi-epoch near-infrared RVs.⁶ Combining these RVs with the parallax and proper motion measured by Gatewood & Coban (2009, assuming 4 mas and 4° errors in their proper motion amplitude and PA, respectively), we derive heliocentric velocities for LP 349-25 of $(U, V, W) = (+4.8 \pm 0.8, -17.2 \pm 1.4, +5.2 \pm 1.3) \text{ km s}^{-1}$ and $(+1.9 \pm 0.4, -11.2 \pm 0.4, -0.5 \pm 0.4) \text{ km s}^{-1}$, respectively. We adopted the sign convention for U that is positive toward the Galactic center and accounted for the errors in the parallax, proper motion, and RV in a Monte Carlo fashion. These space motions place LP 349-25 only 0.7σ or 0.9σ away from the mean of the ellipsoid defined by all other ultracool dwarfs with UVW measurements. (This sample is described in detail in Section 3.4 of Dupuy et al. 2009c.) Using the same method as in our previous work, we have also assessed LP 349-25’s membership in the Galactic thin and thick disk populations using the Besançon model of the Galaxy (Robin et al. 2003), finding at most a 0.3% probability of thick disk membership using the Reiners & Basri (2009) RV and $< 0.1\%$ for the Konopacky et al. (2010) RV. Thus, although the derived space motions are different, the conclusion that LP 349-25 is a normal thin disk member is unaffected. As a likely thin disk member, the age of LP 349-25 is essentially unconstrained by its kinematics. Finally, the fact that LP 349-25 is chromospherically active ($\log(L_{\text{H}\alpha}/L_{\text{bol}}) = -4.52$; Gizis et al. 2000) could potentially provide an age constraint, as the activity of M dwarfs changes with age. However, the long lifetime of activity in such late-M dwarfs found by West et al. (2008) places only a weak constraint of $\lesssim 9$ Gyr for the age of the LP 349-25AB system. Given the measured mass and luminosities of LP 349-25AB, it is in fact likely to be much younger, as discussed in detail in the following sections.

For LHS 1901, there is no published radial velocity, precluding the kinematic analysis described

⁶The discrepancy between these two RV measurements may be due to the fact that Reiners & Basri (2009) measured the RV of the primary component, which would have been near the nadir in its orbital RV curve. Only 65 days prior to the HIRES measurement ($\Delta\text{phase} = 0.02$), Konopacky et al. (2010) measured a primary RV of $-11 \pm 3 \text{ km s}^{-1}$, which is more consistent (at 1.6σ) with the Reiners & Basri (2009) value.

above. The proper motion and parallax of Lépine et al. (2009) provide a measurement of its tangential velocity ($V_{\text{tan}} = 41.1 \pm 1.6 \text{ km s}^{-1}$), indicating that LHS 1901 is typical of late-M dwarfs within 20 pc ($V_{\text{tan}} = 29 \pm 21 \text{ km s}^{-1}$; Faherty et al. 2009) and not likely to be a member of the thick disk or halo populations. Both Reid et al. (2003) and Lépine et al. (2009) have shown that LHS 1901 is not active, which is uncommon for nearby, late-M dwarfs. West et al. (2008) found that activity lifetime increases monotonically with M dwarf spectral type, and for M6 and M7 dwarfs these lifetimes are $7.0 \pm 0.5 \text{ Gyr}$ and $8.0_{-1.0}^{+0.5} \text{ Gyr}$, respectively. Thus, the lack of activity seen in LHS 1901 (M6.5) indicates that its age is likely to be at least as old as 6 Gyr, the 2σ lower limit for the activity lifetime of M6 and M7 dwarfs.

The age of the M2.5 primary star in the Gl 569 triple system has been discussed extensively in the literature. Zapatero Osorio et al. (2004) find that the space motion of Gl 569A places it close to, but not likely a member of, the Ursa Major moving group (300 Myr; Soderblom et al. 1993). However, they suggest that it may be a member of a stream of young A and F stars identified by Chereul et al. (1999), which have ages of 300–800 Myr as derived from Strömgren photometry. Simon et al. (2006) prefer a younger age of 100–125 Myr because Gl 569A seems to lie on the Pleiades sequence in the color–magnitude diagram of Luhman et al. (2005). We have considered whether the X-ray emission from Gl 569A may also place an independent constraint on the age of the system. We computed the X-ray flux of Gl 569A from its *ROSAT* count rate, using the Schmitt et al. (1995) conversion factor, finding $F_X = (3.03 \pm 0.30) \times 10^{-12} \text{ erg cm}^{-2} \text{ s}^{-1}$ ($\log L_X = 28.54$). This lies between the median values of L_X for M dwarfs in the Pleiades (125 Myr) and Hyades (625 Myr) as determined by Preibisch & Feigelson (2005). The X-ray luminosity of Gl 569A is higher than $\approx 75\%$ of Hyades objects and is fainter than $\approx 70\%$ of Pleiades objects. This suggests an intermediate age of $\sim 300\text{--}450 \text{ Myr}$ for the Gl 569 system, although its X-ray luminosity is consistent with the full range of $\sim 125\text{--}625 \text{ Myr}$ at 1σ .

4. Tests of Models

Directly measured dynamical masses enable unique tests of theoretical models of very low-mass stars and brown dwarfs. We consider two independent sets of evolutionary models from the Tucson (Burrows et al. 1997) and Lyon groups (Dusty; Chabrier et al. 2000). Following the approach developed in our previous work (e.g., Liu et al. 2008; Dupuy et al. 2009b), we use the most directly measured properties of our sample binaries (i.e., total mass and individual component luminosities) to derive additional properties (e.g., T_{eff}) from evolutionary models. These model-derived properties are then compared to other available constraints (e.g., from atmospheric model fitting). We note that currently available evolutionary models do not incorporate many of the theoretical advances used in the latest model atmospheres, such as detailed dust cloud models and more accurate molecular and dust opacities. However, our line of analysis is necessarily centered on evolutionary models because we directly measure mass and L_{bol} , not the model atmosphere parameters T_{eff} and $\log(g)$. In addition to this analysis, we also explore the approach recently

utilized by Konopacky et al. (2010) in order to directly compare our results to their findings for the same models.

4.1. Model-derived Ages

As described in detail by Liu et al. (2008) and Dupuy et al. (2009b), the total mass of a binary along with its individual component luminosities can be used to estimate the age of the system from evolutionary models. This age estimate can be quite precise ($\approx 10\%$) when both components are substellar, since the luminosities of brown dwarfs depend very sensitively on age. This is the case for LP 349-25AB: the Lyon and Tucson models give consistent ages of $0.127^{+0.021}_{-0.017}$ Gyr and $0.141^{+0.023}_{-0.019}$ Gyr, respectively (Figure 5, Table 7). The model-derived age of the system is consistent with its kinematics (Section 3.5), and the implications of such a young age for the LP 349-25AB system are addressed in detail in Section 5.

Because LHS 1901AB is composed of two very low-mass stars whose luminosities remain essentially constant over their main-sequence lifetime, the model-derived age for this system is not very precise. Lyon and Tucson models give consistent ages of $0.28^{+9.72}_{-0.08}$ Gyr and $0.37^{+9.63}_{-0.15}$ Gyr, respectively (Table 8). The large upper limits to the age distributions are set by the oldest age for which the model grids are computed (10 Gyr). These broad age distributions are consistent with the age constraint that comes from the lack of chromospheric activity in LHS 1901 (> 6 Gyr; Section 3.5). Because the median model-derived ages are quite young, they would be inconsistent with an age as old as 6 Gyr, but a more precise parallax measurement is needed to test this. For example, if we fix the parallax at its presently measured value but improve its precision from 3.0 mas to 1.0 mas, an attainable goal with seeing-limited astrometry, this age discrepancy would rise to $> 2\sigma$ significance for the Lyon models.

Gl 569Bab has a higher mass than LP 349-25AB but lower component luminosities, and thus the Lyon and Tucson models give older ages of $0.46^{+0.11}_{-0.07}$ Gyr and $0.51^{+0.13}_{-0.08}$ Gyr, respectively (Figure 5, Table 9). These are consistent with the age constraints from Gl 569A discussed in Section 3.5, with the exception of the age of 100–125 Myr proposed by Simon et al. (2006) based on its position on the color–magnitude diagram. Given the unavailability of such data for M dwarfs at ~ 500 Myr, we suggest that Gl 569A may well be consistent with such an older age. Our model-derived age for the Gl 569Bab system is also in agreement with the age estimates from Lane et al. (2001) and Zapatero Osorio et al. (2004).

4.2. Individual Masses

All of our target binaries have flux ratios near unity, thus enabling robust individual mass estimates with only a very weak dependence on model assumptions. For LHS 1901AB, the Lyon and Tucson models give mass ratios ($q \equiv M_B/M_A$) of $0.958^{+0.015}_{-0.014}$ and $0.966^{+0.011}_{-0.016}$, respectively. Thus,

the model-derived individual masses (listed in Table 8) are nearly identical, and their precision is dominated by the ${}_{-11}^{+13}\%$ uncertainty in M_{tot} .

Because the model-derived ages for LP 349-25AB are quite young, the inferred mass ratios are somewhat further from unity than they would otherwise be for the measured 0.133 ± 0.019 dex luminosity ratio. The Lyon and Tucson models give consistent mass ratios of $0.872_{-0.018}^{+0.014}$ and $0.863_{-0.019}^{+0.013}$, respectively. This results in individual masses of $0.064_{-0.004}^{+0.005} M_{\odot}$ and $0.056 \pm 0.004 M_{\odot}$ for the components of LP 349-25AB (Lyon), placing both below the substellar boundary ($\sim 0.070 M_{\odot}$; Chabrier et al. 2000) and LP 349-25B likely below the lithium depletion boundary ($\approx 0.055\text{--}0.065 M_{\odot}$; Chabrier & Baraffe 1997). Konopacky et al. (2010) reported resolved RV measurements for LP 349-25AB and, combined with their astrometric orbit, found $q = 2.0_{-0.7}^{+3.0}$. This is nominally inconsistent with our model-derived mass ratio at 1.6σ , with their value corresponding to the secondary being *more* massive than the primary. In Figure 6, we show their measurements along with the RV curve predicted for mass ratios of 0.87 and 2.0, assuming their best-fit center-of-mass velocity of $-8.0 \pm 0.5 \text{ km s}^{-1}$. Fixing the orbital elements to the values from the astrometric orbit, we find χ^2 values for the RV measurements that are unreasonably small for both values of q ($\chi^2 = 0.5$ for $q = 2.0$ and $\chi^2 = 1.7$ for $q = 0.87$; 6 DOF). This implies that the errors on the RV measurements are overestimated, and within these large errors both values of the mass ratio (0.87 and 2.0) are acceptable. We discuss the plausibility of these different mass ratios in detail in Section 5.

For Gl 569Bab, the Lyon and Tucson models give consistent mass ratios of $0.866_{-0.014}^{+0.019}$ and $0.886_{-0.017}^{+0.021}$, respectively. This agrees with the spectroscopically determined mass ratio of $0.71_{-0.13}^{+0.19}$ from Konopacky et al. (2010). Our slightly higher model-derived mass ratio results in somewhat more similar masses (0.075 ± 0.004 and $0.065_{-0.004}^{+0.005} M_{\odot}$, Lyon) than implied by the directly measured mass ratio ($0.082_{-0.009}^{+0.008}$ and $0.059_{-0.007}^{+0.009} M_{\odot}$). In both cases however, Gl 569Bb is expected to lie near the mass-limit for lithium burning, which can be tested directly in the future with resolved optical spectroscopy of the Li I doublet at 6708 Å. In addition, absolute astrometric monitoring of the 2.4-yr orbital period binary can readily yield a refined measurement of the mass ratio: 1 mas astrometry would give a 5% mass ratio error, $\sim 4\times$ better than spectroscopy.

4.3. Temperatures and Surface Gravities

Effective temperature (T_{eff}) is one of the most difficult properties to measure directly, as it requires a direct measurement of the radius and luminosity. To date, radius measurements remain elusive for very low-mass stars and brown dwarfs in the field. Thus, when testing model predictions we are restricted to consistency checks between different methods of estimating T_{eff} . In Section 3.4, we estimated the temperatures of the primary components of our sample binaries by fitting their integrated-light spectra with atmospheric models. The best-fit Drift-PHOENIX and Gaia-Dusty model spectra are shown in Figure 7 plotted over the observed spectra. Evolutionary models provide a nearly independent temperature estimate by providing a prediction of the radius, which yields

T_{eff} when combined with the measured L_{bol} .⁷

For LHS 1901A and LHS 1901B, Lyon evolutionary models give effective temperatures of 2860 ± 50 K and 2820^{+50}_{-40} K, respectively, and the Tucson evolutionary models give 100 K warmer temperatures of 2960 ± 30 K and 2930^{+30}_{-40} K. Both sets of models give consistent surface gravities of $\log(g) = 5.2$ (cgs) for both components. All NIR atmospheric model fits gave systematically higher temperatures of 3000–3100 K and surface gravities near the predicted value (5.0 ± 0.5 dex). Given the nominal uncertainty (i.e., the model atmosphere grid step) of 100 K in the best-fit T_{eff} values, the largest discrepancy of ≈ 150 K with the Lyon evolutionary models is marginally significant. To provide an additional point of comparison for the T_{eff} estimates, we compiled all M6.5 and M7 dwarfs with effective temperatures derived by Gautier et al. (2007) using the nearly model-independent infrared flux method (Blackwell & Shallis 1977). We found a mean and standard deviation of 2710 ± 30 K for these objects, which is lower than T_{eff} estimates from both classes of models by 140–290 K, agreeing somewhat better with evolutionary models.

For LP 349-25A and LP 349-25B, Lyon models give effective temperatures of 2660 ± 30 K and 2520 ± 30 K, respectively, and the Tucson models give 120 K warmer temperatures of 2780 ± 30 K and 2640 ± 30 K. Lyon models predict surface gravities of about 4.9 (cgs) for both components, and Tucson models predict 5.0 (cgs). In comparison, atmospheric model fits of LP 349-25A gave 2800–3000 K and surface gravities near the predicted value (5.0 ± 0.5 dex).⁸ Again, the Tucson evolutionary model T_{eff} is consistent with that derived from atmospheric models, while the Lyon evolutionary models are lower by ≈ 150 K.

For Gl 569Ba and Gl 569Bb, Lyon models give effective temperatures of 2430 ± 30 K and 2210 ± 30 K, respectively, and the Tucson models give 100 K warmer temperatures of 2530 ± 30 K and 2300 ± 30 K. Lyon models predict surface gravities of about 5.2 (cgs) for both components, and Tucson models predict 5.3 (cgs). In comparison, atmospheric model fits of Gl 569Ba gave 2700–2900 K, with a wide range of surface gravities ($\log(g) = 4.5$ to 6.0). These T_{eff} values are much higher than evolutionary models by 150–250 K, and the broad range of surface gravities is in reasonable agreement.

In order to understand why temperature estimates from the two classes of models typically do not agree, we show our observed spectra in Figure 8 plotted with Drift-PHOENIX and Gaia-Dusty model spectra that have T_{eff} and $\log(g)$ values closest to the Lyon Dusty evolutionary model-

⁷Nearly independent because evolutionary models use theoretical atmospheres as boundary conditions when evaluating hydrostatic equilibrium and the amount of energy being released. This can result in radius deviations of up to $\approx 10\%$ when comparing dustless to extremely dusty model atmospheres at low temperatures ($T_{\text{eff}} \lesssim 2000$ K), but the effect is $< 1\%$ at the warmer temperatures of late-M dwarfs (see Figure 2 of Chabrier et al. 2000).

⁸We note that all SED fits including the 0.81 to 0.95 μm optical segment gives a surface gravity of 4.0 (cgs) for LP 349-25A, which is highly discrepant with the evolutionary model value of 5.0 (cgs). This would require an unrealistic radius of $\approx 0.4 R_{\odot}$ given the known mass of LP 349-25A. Such an unrealistic surface gravity is also found from the Ames-Dusty models for LHS 1901A.

derived values. This enables us to assess what spectral features prevented our fitting procedure from selecting these model spectra, which are very similar to the spectra used for the atmospheric boundary condition in the Lyon models.⁹ The NIR SED fits do not seem to be significantly affected by broadband colors (e.g., the better fitting models do not necessarily have $J - K$ colors closer to what is observed). Rather, the shapes of the spectra, which are sculpted by broad molecular absorption bands, seem to determine the best-fit models.

- The disagreement in shape is most pronounced at H band, where the observed spectrum is much flatter than the low- T_{eff} , low-gravity model spectra that would better correspond to evolutionary model-derived properties. This could be due partly to missing FeH opacity in the models between ~ 1.5 and $1.7 \mu\text{m}$ (Reid et al. 2001; Wallace & Hinkle 2001; Cushing et al. 2003).
- The observed K -band shape is also flatter (i.e., the band peak at $2.2 \mu\text{m}$ is more suppressed) than in the low- T_{eff} , low-gravity model spectra.
- In J band, the fit seems to be driven by the deep H_2O absorption band at $1.33 \mu\text{m}$, which is too deep in the low- T_{eff} , low-gravity model spectra.
- In Y band, the FeH 0–0 bandhead at $0.99 \mu\text{m}$ is too strong in the spectra corresponding to evolutionary model-derived properties. This could alternatively be interpreted as the overall continuum at Y band being too high in the atmospheric models (e.g., missing opacity from wings of resonant alkali lines such as K I).

In general, we have found that atmospheric models predict systematically higher effective temperatures than evolutionary models.¹⁰ This pattern is illustrated in Figure 9, which shows the T_{eff} estimates from each class of models plotted against each other. A systematic shift of ≈ 250 K would bring the models into agreement, with either the atmospheric model estimates being too warm or the evolutionary model estimates too cool (i.e., model radii too large by 15–20%).¹¹ We note that the observed discrepancy cannot simply be due to the fact that our method relies on fitting

⁹The Ames-Dusty model atmospheres provided the spectra used for the boundary condition in the Lyon Dusty evolutionary models. However, we choose to show the Gaia-Dusty models for comparison as their SEDs are very similar but with updated line lists (Table 5). This enables us to identify remaining problems and not dwell on issues that have already been resolved in the latest generation of that model grid.

¹⁰Rice et al. (2010) have recently fit model atmospheres to high- and medium-resolution J -band spectra of mid- to late-M dwarfs. Most of their sample are young M dwarfs ($\lesssim 10$ Myr), but for their three field M7 to M9 dwarfs they find higher T_{eff} values than previously published estimates based on measured luminosities and estimated radii for objects of similar spectral type. Thus, their findings are consistent with our results.

¹¹ Interestingly, the SED fits that include the wavelength segment from 0.81 to $0.95 \mu\text{m}$ (which are less preferred for reasons described in Section 3.4) give T_{eff} values ≈ 100 K more consistent with evolutionary models. This indicates that optical diagnostics utilizing TiO bandhead strengths (e.g., see Mohanty et al. 2004) may be needed to provide more accurate T_{eff} estimates than can be obtained from near-infrared spectroscopy alone.

the integrated-light spectra of binaries. As discussed in Section 3.4, if the secondary component’s flux impacted the best-fit model it would have the effect of lowering the derived T_{eff} , whereas we find temperatures that are too warm. This means that the discrepancy could only be larger than we observe. In addition, even a significant nonsolar metallicity for our binaries could not explain the observed temperature offset, as Bowler et al. (2009) showed that models of varying metallicity gave the same best-fit T_{eff} to within the model grid step of 100 K for the ultracool subdwarf HD 114762B (d/sdM9).

We have considered what systematic errors could contribute to this discrepancy between evolutionary and atmospheric models. Currently available evolutionary models use much older versions of model atmospheres as their boundary condition, and this could potentially result in systematic errors in their output. Saumon & Marley (2008) calculated evolutionary models both with and without the effects of dust clouds in the atmosphere and found at worst 6% differences in the resulting radii, which is much lower than what is needed to account for our observed discrepancy. We can also estimate how other input assumptions impact evolutionary model output simply by comparing the predictions of the Lyon and Tucson models, which use different helium abundances, model atmospheres, and dust treatment. These two sets of models predict radii different by 7–10% and temperatures different by ≈ 100 K for the objects in our sample – more than a factor of two lower than what is needed to fully account for the observed discrepancy. Presently available model atmospheres are more advanced than evolutionary models, but as shown in Figure 7 they cannot completely match our observed near-infrared spectra. Therefore, the resulting temperature values must harbor systematic errors at some level. Thus, we conclude that the model atmospheres must be responsible for at least part of the observed 250 K discrepancy. In fact, we suggest that the atmospheric models are more likely than the evolutionary models to be the primary source of the discrepancy, since roughly the same T_{eff} offset is observed over a wide range of masses, ages, and activity levels but the same temperature range. This proposition will be readily testable with eclipsing binary measurements given the large implied radius difference between models (15–20%).

4.4. Near-Infrared Colors

We computed resolved photometry for our sample binaries in the MKO photometric system to compare to Lyon model predictions. For Gl 569Bab, we used our integrated-light MKO photometry described in Section 2.1 along with the best available flux ratios from Table 2. For LP 349-25 and LHS 1901, we first converted their integrated-light 2MASS photometry to the MKO system by deriving correction terms from our near-infrared spectra. The resulting component magnitudes for all three binaries are listed in Table 4. Near-infrared colors on the MKO photometric system were derived from the Lyon models in the same fashion as other properties (e.g., T_{eff}), and the results are listed in Tables 7, 8, and 9. In Figures 10 and 11, we show the photometry of LP 349-25AB and Gl 569Bab compared to Lyon mass tracks computed for the individual masses of both components. The observed $JHKL'$ photometry is significantly discrepant with model tracks at all ages, with

models typically predicting ≈ 0.1 – 0.2 mag bluer JHK colors than observed and ≈ 0.1 – 0.2 mag redder $K - L'$ colors. For LHS 1901AB, the JHK colors predicted by models are in much better agreement with the observations. The most discrepant color is $H - K$, which is only 0.07 mag (2.3σ) redder than predicted, and this may be due to missing FeH opacity in the H band. (We do not show a corresponding figure for LHS 1901AB as its components are main-sequence stars that evolve at essentially constant color.)

4.5. An Alternative Approach: Model-derived Properties Using L_{bol} and T_{eff}

Konopacky et al. (2010) have recently described an approach to test models of ultracool dwarfs with dynamical mass measurements that is somewhat different from ours. They use the measured individual luminosities along with T_{eff} estimates for each component to derive any other property (e.g., M_{tot} or age) from evolutionary models. (Their T_{eff} estimates are derived by fitting model atmospheres to resolved broadband photometry of the binaries.) This approach is similar to ours in that it uses two quantities to determine a third from evolutionary models, which is necessary because brown dwarfs occupy a mass– L_{bol} –age (or T_{eff} – L_{bol} –age) relation instead of the simpler mass– L_{bol} relation for stars on the main sequence. In Liu et al. (2008), we considered in detail such model tests using different combinations of these fundamental parameters, and we ultimately chose to use mass and L_{bol} to derive other properties as these are the most directly measured quantities. However, any discrepancies we have found in the models should also manifest themselves in the T_{eff} – L_{bol} approach that has been adopted by Konopacky et al. (2010). In this section, we examine the results of analyzing our late-M dwarf measurements using the Konopacky et al. (2010) approach.

We first interpolated the Lyon and Tucson model grids at individual (T_{eff} , L_{bol}) points in the same fashion as Konopacky et al. (2010), with our temperatures coming from the Gaia-Dusty atmospheric model fitting of the NIR SED as described in Section 3.4. (This is the exact same model atmosphere grid as used by Konopacky et al. 2010.) In order to compute uncertainties in the model-derived properties using this approach, we used 10^3 luminosity and temperature values randomly drawn from normal distributions corresponding to the measurement errors. We assumed 100 K errors in T_{eff} , equal to the model atmosphere grid step. The resulting evolutionary model-derived masses are plotted in Figure 12 against those derived by Konopacky et al. (2010).

Our masses are significantly higher than theirs by about a factor of ~ 2 to 4 because our T_{eff} estimates are systematically higher while their luminosity measurements are very similar to ours. In order for models to match our much higher temperatures at similar luminosities, the masses must be larger and the ages somewhat older. The best illustration of this disagreement is the case of 2MASS J2206–2047A, as Konopacky et al. (2010) used essentially identical luminosities and photometry as Dupuy et al. (2009a), and the component fluxes are nearly identical, removing any ambiguity in fitting its integrated-light spectrum. Konopacky et al. (2010) found 2350 ± 80 K from fitting its resolved broadband photometry, while our best-fit spectrum from the very same grid of model atmospheres has a temperature of 2900 ± 100 K. Therefore, despite the other similarities in our

inputs, we found a primary mass of $0.090_{-0.006}^{+0.006} M_{\odot}$ using the Lyon Dusty evolutionary models, while they found $0.047_{-0.012}^{+0.016} M_{\odot}$. Neither of these masses agrees with the measured mass ($0.077_{-0.017}^{+0.012} M_{\odot}$, Table 7 of Dupuy et al. 2009a): our mass is higher, and the Konopacky et al. (2010) mass is much lower. The differences between our derived masses for LP 349-25A and Gl 569Ba are even larger, as Konopacky et al. (2010) found extremely low masses for these objects ($0.02 \pm 0.02 M_{\odot}$ and $0.02_{-0.01}^{+0.02} M_{\odot}$, respectively).¹²

Fundamentally, both the Konopacky et al. (2010) approach and our standard method to test models provide similar information: a consistency check on the temperatures from atmospheric and evolutionary models. The comparison presented here highlights how the amplitude, and even the sign, of discrepancies found between measured and model-predicted masses depend strongly on the input temperature estimates. Using the exact same atmospheric model grids, but different methods, our two groups have arrived at values of T_{eff} different by ≈ 650 K. This is due to the fact that the fitting method of Konopacky et al. (2010) relies solely on the broadband colors of models, whereas our method is driven by the shape of specific spectral features. As shown in Figure 10 and in our previous work (Liu et al. 2008; Dupuy et al. 2009a,b,c), the broadband colors of models consistently disagree with observations of objects of known mass over a broad range of spectral types. We also note that a significant disadvantage of the Konopacky et al. (2010) $L_{\text{bol}}-T_{\text{eff}}$ approach is that evolutionary models occupy a very thin strip in this parameter space as opposed to $L_{\text{bol}}-M$. This resulted in many of our randomly drawn $(L_{\text{bol}}, T_{\text{eff}})$ measurements falling outside the range predicted by models (from 1.2% to 99.8% in the worst case), and we simply excluded these points from the analysis.

Konopacky et al. (2010) interpreted their observed discrepancies with theory as an error in the evolutionary model cooling curves, i.e., a mass problem. Using their method, we find an opposite mass discrepancy because our T_{eff} estimates are ≈ 650 K higher than theirs, resulting in higher masses. We suggest that the strong sensitivity of this model-testing method to the input T_{eff} estimates means that any observed discrepancies more readily identify problems in the way T_{eff} is determined from atmospheric models (i.e., a temperature problem), rather than a problem with evolutionary models.

5. The Nature of LP 349-25AB

It is somewhat surprising that LP 349-25AB has turned out to be a pair of young (~ 140 Myr) brown dwarfs given the lack of detectable lithium (Reiners & Basri 2009) and its $M8.0 \pm 0.5$ spectral classification (Gizis et al. 2000). With a total mass of $0.120_{-0.007}^{+0.008} M_{\odot}$, one or both of the components may even lie below the theoretically predicted lithium depletion boundary at $\approx 0.055-$

¹²We note that the extremely low model-derived masses of $\approx 20 M_{\text{Jup}}$ reported by Konopacky et al. (2010) imply very young ages that are inconsistent with the lack of any low-gravity signatures in these objects' spectra.

0.065 M_{\odot} . In fact, even objects massive enough to deplete lithium take time to achieve the internal temperature necessary to do so ($\approx 2 \times 10^6$ K; Pozio 1991). For example, Chabrier et al. (1996) show that a 0.070 M_{\odot} object takes 220 Myr to destroy 99% of its initial lithium, while at 145 Myr only $> 0.080 M_{\odot}$ stars are similarly depleted. Using the Lyon and Tucson models, we find predicted lithium fractions of $0.68_{-0.42}^{+0.24}$ and $0.75_{-0.52}^{+0.15}$ for LP 349-25A, respectively, and $0.95_{-0.18}^{+0.04}$ and $0.96_{-0.08}^{+0.03}$ for LP 349-25B. Thus, both sets of models predict that the primary may be depleted in lithium, but that the secondary should retain nearly all of its initial lithium. The presence of lithium in the fainter secondary may be masked by the primary flux in the integrated-light spectroscopy of the system, so resolved spectroscopy to detect the Li I doublet at 6708 Å is needed to test this prediction of brown dwarf evolutionary models directly.

Evolutionary models make very precise predictions for the age of LP 349-25AB from its measured total mass and individual luminosities. Taken together, the Lyon and Tucson models predict an age of 140 ± 30 Myr. This is consistent with the age of 125 Myr derived for the Pleiades by Stauffer et al. (1998) using the lithium depletion boundary. Thus, we might expect LP 349-25AB to obey roughly the same boundaries in spectral type and color as found by Stauffer et al. (1998). The lithium boundary in the Pleiades lies between spectral types of M6.5 and M7, with objects \geq M7 having detectable lithium. Although the spectral type determinations for the components of LP 349-25AB are hampered by the lack of resolved spectroscopy, the measured integrated-light type of $M8.0 \pm 0.5$ makes it unlikely that LP 349-25A is earlier than M7, yet it is clearly depleted in lithium. Stauffer et al. (1998) used spectroscopically derived ($R - I$) colors to define the lithium depletion boundary in the Pleiades, with all objects bluer than 2.20 mag being depleted in lithium. From the integrated-light optical spectrum of Reid et al. (2003), we derived ($R - I$) = 2.50 mag using the same method as Stauffer et al. (1998).¹³ At this color index, all brown dwarfs in the Pleiades sample of Stauffer et al. (1998) show evidence for the presence of lithium.

LP 349-25A thus stands out as potentially anomalous compared to determination of the lithium boundary in the Pleiades. (Note that our comparison is purely empirical in nature and does not depend on any theoretical assumptions regarding lithium depletion in brown dwarfs.) This indicates that there may be a problem with the model-derived age for LP 349-25AB. At older ages, the lithium depletion boundary moves to lower masses (i.e., later spectral types), so an older age for LP 349-25AB would bring it into better agreement with the Pleiades. The age derived in our analysis is based solely on the model-predicted L_{bol} evolution, and for its actual age to be older either: (1) the measured parallax would have to be smaller (i.e., LP 349-25AB more distant); or (2) the models would need to under-predict the luminosities of LP 349-25AB. In the former case, a parallax that is 3.5σ smaller (placing the binary at 14.3 ± 0.3 pc) would increase the total mass to 0.152 M_{\odot} , resulting in a model-derived age 190 ± 50 Myr and individual components predicted to

¹³The method used by Stauffer et al. (1998) was calibrated against M dwarfs in the Gliese catalog (Gliese & Jahreiss 1991), and the scatter in (R-I) color at a given M subtype is 0.07 to 0.14 mag. Therefore, we estimate the uncertainties in spectroscopically derived values of ($R - I$) to be ≈ 0.10 mag.

be nearly fully depleted in lithium. In the latter case, the luminosities we measure would indeed be high for their mass, not because the objects are very young but rather because model L_{bol} evolution is not correct. Such an error has previously been suggested by Dupuy et al. (2009b) to explain the higher-than-predicted luminosities of the benchmark brown dwarf binary HD 130948BC (L4+L4). An independent measurement of the parallax for LP 349-25AB and resolved optical spectroscopy is needed to better assess this possible discrepancy with brown dwarfs in the Pleiades.

The youth of LP 349-25AB could potentially be reflected in low-gravity spectral features such as have been noted for other field ultracool dwarfs (e.g., McGovern et al. 2004; Allers et al. 2007; Kirkpatrick et al. 2008; Rice et al. 2010). The integrated-light optical spectrum from Reid et al. (2003) and our near-infrared spectrum do not show obvious hallmarks of low surface gravity. However, near-infrared spectra of M7 and M8 dwarfs in the Pleiades recently published by Bihain et al. (2010) also show no distinguishing characteristics relative to field dwarfs of the same spectral type, at least at low resolution, $R \sim 50$, and modest S/N . We have also checked for possible association of LP 349-25AB with young moving groups using our derived (U, V, W) heliocentric space velocity (Section 3.5). We find no such association with any of the groups listed by Zuckerman & Song (2004) and Torres et al. (2008).

LP 349-25AB is one of the relatively few ultracool dwarfs that displays radio emission ($\sim 10\%$ occurrence rate for $>M7$ dwarfs; Berger 2006). Phan-Bao et al. (2007) discovered the radio emission from LP 349-25AB at 8.5 GHz but with a beam size of $9''.2 \times 8''.0$ were unable to resolve the binary to determine whether both components are radio-luminous. Osten et al. (2009) presented additional unresolved, multi-frequency, multi-epoch observations to better constrain the emission mechanism, finding a lack of variability in both the radio flux and spectral index on both short (hours) and long (months) timescales. Their observations spanning 10.7 hours would have easily captured multiple rotations of the emitting component, as the measured $v \sin(i)$ of $56 \pm 6 \text{ km s}^{-1}$ (Reiners & Basri 2010) implies a maximum rotation period of $2.9/\sin(i)$ hours (assuming an average model-derived radius of $0.136 R_{\odot}$) or a period of 2.6 hours if the rotation axis is co-aligned with the binary orbit. LP 349-25AB is the only known radio-luminous ultracool dwarf that does not display some level of variability. To explain all observed radio properties, Osten et al. (2009) favored a long-lived ($\gtrsim 0.6 \text{ yr}$), high-latitude (i.e., polar) source emitting gyrosynchrotron radiation. Future observations at higher angular resolution using the Extended Very Large Array are needed to determine whether only one or both components are radio-luminous. Our dynamical mass measurement will be a key input in developing customized models to better understand the origin of the magnetic structures generating the unique radio emission of LP 349-25AB.

Finally, we consider the possibility that LP 349-25AB is actually a higher order multiple system. The resolved colors and magnitudes of the two components are consistent with a simple binary as the secondary is slightly fainter and redder than the primary. As discussed in Section 4.2, we find that the resolved radial velocity measurements of Konopacky et al. (2010) are consistent with both the model-derived mass ratio of 0.87 and their best fit value of 2.0, in which the secondary has twice the mass of the primary. In this scenario, the B component would have to actually comprise

two fainter brown dwarfs whose combined luminosity is below that of the single A component.¹⁴ However, in this case the A component’s mass would only be about $0.04 M_{\odot}$, which is well below the lithium depletion limit and thus LP 349-25 should display detectable lithium absorption. In addition, dividing the binary into a higher order multiple would necessarily require the age to be younger for such lower mass component objects to output the same amount of energy. At younger ages, it would be even less likely that the most massive component (whatever its mass) would have had time to reach the core temperature needed to destroy its initial lithium. Thus, we conclude that given all available constraints LP 349-25AB cannot be a higher order multiple.

6. Conclusions

We have determined the orbits of three late-M binaries from Keck NGS and LGS AO orbital monitoring. From observations spanning 5.9 years (75%) of the 7.8 yr orbit of LP 349-25AB, we have determined a total mass of $0.120^{+0.008}_{-0.007} M_{\odot}$. For LHS 1901AB, we have found a highly eccentric ($e = 0.830 \pm 0.005$) 16.1-yr orbit from observations spanning 5.9 years (36% of the orbit, including periastron passage), deriving a dynamical mass of $0.194^{+0.025}_{-0.021} M_{\odot}$. We have also determined a new orbit for Gl 569Bab based solely on astrometrically well-calibrated instruments (Keck/NIRC2 and *HST*/STIS), finding a larger semimajor axis and thus larger dynamical mass ($0.140^{+0.009}_{-0.008} M_{\odot}$) than previous work. For all binaries, the most significant contribution to their mass uncertainties are the errors in their parallaxes.

Despite LP 349-25AB’s integrated-light spectral type of M8 *and* lack of detectable lithium absorption, this binary has turned out to be pair of brown dwarfs. To match the observed total mass and component luminosities, evolutionary models predict that the system must be quite young (140 ± 30 Myr) and that at least the secondary component should have retained most of its initial lithium. If the model-derived age for LP 349-25AB is correct, it is nearly the same age as the Pleiades; however, it appears to be discrepant with the boundary between lithium-depleted and lithium-bearing objects from Stauffer et al. (1998). If the parallax measured by Gatewood & Coban (2009) is accurate, this disagreement with the Pleiades indicates a possible problem with the model-derived age, which in our analysis is based solely on the predicted L_{bol} evolution. An older age for LP 349-25AB would remedy this problem, as the lithium depletion boundary moves to later spectral types at older ages. This solution would require that models under-predict the luminosities of brown dwarfs, which has previously been suggested by Dupuy et al. (2009b) to explain the higher-than-predicted luminosities of the benchmark brown dwarf binary HD 130948BC (L4+L4). We also find that the lack of lithium depletion in at least the primary component effectively rules out the possibility that LP 349-25AB is a higher order multiple.

¹⁴Another possibility resulting in $q = 2.0$ that can be ruled out is that the secondary component of LP 349-25AB is more luminous than the primary. As shown in Figure 1 of Burrows et al. (2001), a secondary with a putative mass of $0.04 M_{\odot}$ would never outshine the primary, even during its deuterium-fusing phase at ≈ 2.5 Myr.

As in our previous work (e.g., Liu et al. 2008; Dupuy et al. 2009b), we have used measured dynamical masses to test the predictions of evolutionary and atmospheric models. Properties such as T_{eff} and $\log(g)$ are derived from evolutionary models using only M_{tot} and the resolved component luminosities. We have also fit model atmospheres to the integrated-light 0.95–2.42 μm spectra as an independent method for estimating T_{eff} . Including our previous work on 2MASS J2206–2047AB (Dupuy et al. 2009a), there is now a sample of four late-M binaries with precise dynamical masses and near-infrared spectra enabling a consistency check between evolutionary model-derived properties and model atmospheres. All four model atmosphere grids we tested give effective temperatures ≈ 250 K warmer than predicted for our objects of known mass from Lyon Dusty evolutionary model radii (including the Ames-Dusty model atmospheres which were used as the boundary condition for the Dusty evolutionary models).

Although model atmospheres now incorporate considerably more advanced theory than the decade-old evolutionary models, we propose that such a large offset cannot be entirely explained by problems with model radii. Instead, model atmospheres are likely to be the major source of this discrepancy given that: (1) they must harbor systematic errors at some level, since they do not completely match our observed spectra; and (2) roughly the same T_{eff} offset is observed over a narrow range of T_{eff} but a wide range of masses, ages, and activity levels. Such a discrepancy would be difficult to explain in the context of evolutionary models, although they may also harbor systematic errors that partially contribute to this inconsistency. Directly measured radii are needed to determine which set of models correctly predicts T_{eff} (if either do). This can be readily tested with future discoveries of late-M eclipsing binaries, as a 250 K offset corresponds to a substantial radius difference (15–20%).

In addition to our standard line of analysis, we have also explored the approach to testing models used by Konopacky et al. (2010) for the late-M binaries common to our two samples. Our model atmosphere fitting of integrated-light spectra yields higher T_{eff} estimates than their approach of fitting resolved broadband photometry. Consequently, we find evolutionary model-derived masses from their approach that are a factor of ~ 2 to 4 higher than theirs, resulting in an opposite discrepancy with measured dynamical masses. This illustrates that their method sensitively relies upon the input T_{eff} , a property that cannot be determined directly without radius measurements. Thus, this approach may have limited utility in testing evolutionary models, as observed discrepancies are more readily caused by problems with T_{eff} estimates from model atmospheres. To summarize how our conclusions contrast with those of Konopacky et al. (2010): (1) They found estimates for T_{eff} from model atmospheres that are ≈ 400 K *lower* than our evolutionary model-derived values, whereas we find T_{eff} estimates that are ≈ 250 K *higher*. (2) They interpreted these results in terms of mass, concluding that systematic errors in the evolutionary model cooling curves were responsible for observed discrepancies. We propose instead that the discrepancy is largely caused by systematic errors in the model atmospheres.

As the sample of ultracool dwarfs with dynamical mass measurements grows, we are beginning to probe the diversity of the field population, which comprises both very low-mass stars and brown

dwarfs. At the cool temperatures of late-M dwarfs, field objects can span nearly a factor a two in mass depending on their age, which makes mass measurements crucial for breaking this degeneracy. At cooler temperatures there are even fewer mass measurements presently available, and the effects of complex processes such as atmospheric dust formation become more important. Therefore, continued orbital monitoring will be imperative to bring similar tests of models as we report here into the much cooler regimes of the L and T dwarfs.

It is a pleasure to thank Joel Aycock, Randy Campbell, Al Conrad, Heather Hershley, Jim Lyke, Jason McIlroy, Gary Punawai, Julie Riviera, Hien Tran, Cynthia Wilburn, and the Keck Observatory staff for assistance with the Keck observations. We are very grateful to Michal Simon and Chad Bender for providing us with their Keck/NIRC2 images of Gl 569Bab. We also thank France Allard for providing evolutionary models with near-infrared photometry on the MKO system, Travis Barman for providing us with the Gaia-Dusty model spectra, Kelle Cruz for providing the optical spectrum of LP 349-25, Adam Burgasser for providing the SpeX prism spectrum of Gl 569A, Brian Cameron for making available his NIRC2 distortion solution, and Céline Reylé for customized Besançon Galaxy models. We are indebted to Katelyn Allers for assistance in obtaining IRTF/SpeX data of Gl 569B. Our research has employed the 2MASS data products; NASA’s Astrophysical Data System; the SIMBAD database operated at CDS, Strasbourg, France; and the M, L, and T dwarf compendium housed at <http://www.DwarfArchives.org> and maintained by Chris Gelino, Davy Kirkpatrick, and Adam Burgasser (Kirkpatrick 2003; Gelino et al. 2004). MCL, TJD, and BPB acknowledge support for this work from NSF grants AST-0507833 and AST-0909222. Finally, the authors wish to recognize and acknowledge the very significant cultural role and reverence that the summit of Mauna Kea has always had within the indigenous Hawaiian community. We are most fortunate to have the opportunity to conduct observations from this mountain.

Facilities: Keck II Telescope (LGS AO, NIRC2), CFHT (PUEO, KIR), VLT (NACO), IRTF (SpeX)

REFERENCES

- Allard, F., Hauschildt, P. H., Alexander, D. R., Tamanai, A., & Schweitzer, A. 2001, *ApJ*, 556, 357
- Allers, K. N., et al. 2007, *ApJ*, 657, 511
- Asplund, M., Grevesse, N., & Sauval, A. J. 2005, in *Astronomical Society of the Pacific Conference Series*, Vol. 336, *Cosmic Abundances as Records of Stellar Evolution and Nucleosynthesis*, ed. T. G. Barnes III & F. N. Bash, 25
- Barber, R. J., Tennyson, J., Harris, G. J., & Tolchenov, R. N. 2006, *MNRAS*, 368, 1087
- Barrado y Navascués, D., Stauffer, J. R., & Patten, B. M. 1999, *ApJ*, 522, L53

- Berger, E. 2006, *ApJ*, 648, 629
- Bernath, P. 2006, in *American Institute of Physics Conference Series*, Vol. 855, *Astrochemistry - From Laboratory Studies to Astronomical Observations*, ed. R. I. Kaiser, P. Bernath, Y. Osamura, S. Petrie, & A. M. Mebel, 143–148
- Bihain, G., Rebolo, R., Zapatero Osorio, M. R., Béjar, V. J. S., & Caballero, J. A. 2010, *A&A*, in press (astro-ph/1005.3249)
- Blackwell, D. E., & Shallis, M. J. 1977, *MNRAS*, 180, 177
- Bowler, B. P., Liu, M. C., & Cushing, M. C. 2009, *ApJ*, 706, 1114
- Brott, I., & Hauschildt, P. H. 2005, in *ESA Special Publication*, Vol. 576, *The Three-Dimensional Universe with Gaia*, ed. C. Turon, K. S. O’Flaherty, & M. A. C. Perryman, 565
- Burrows, A., Hubbard, W. B., Lunine, J. I., & Liebert, J. 2001, *Reviews of Modern Physics*, 73, 719
- Burrows, A., et al. 1997, *ApJ*, 491, 856
- Burrows, A., Ram, R. S., Bernath, P., Sharp, C. M., & Milsom, J. A. 2002, *ApJ*, 577, 986
- Burrows, A., & Volobuyev, M. 2003, *ApJ*, 583, 985
- Chabrier, G., & Baraffe, I. 1997, *A&A*, 327, 1039
- Chabrier, G., Baraffe, I., Allard, F., & Hauschildt, P. 2000, *ApJ*, 542, 464
- Chabrier, G., Baraffe, I., & Plez, B. 1996, *ApJ*, 459, L91
- Chereul, E., Crézé, M., & Bienaymé, O. 1999, *A&AS*, 135, 5
- Close, L. M., Siegler, N., Freed, M., & Biller, B. 2003, *ApJ*, 587, 407
- Cruz, K. L., Reid, I. N., Liebert, J., Kirkpatrick, J. D., & Lowrance, P. J. 2003, *AJ*, 126, 2421
- Cushing, M. C., et al. 2008, *ApJ*, 678, 1372
- Cushing, M. C., Rayner, J. T., Davis, S. P., & Vacca, W. D. 2003, *ApJ*, 582, 1066
- Cushing, M. C., Rayner, J. T., & Vacca, W. D. 2005, *ApJ*, 623, 1115
- Cushing, M. C., Vacca, W. D., & Rayner, J. T. 2004, *PASP*, 116, 362
- Cutri, R. M., et al. 2003, *2MASS All Sky Catalog of point sources*. (The IRSA 2MASS All-Sky Point Source Catalog, NASA/IPAC Infrared Science Archive. <http://irsa.ipac.caltech.edu/applications/Gator/>)

- Diolaiti, E., Bendinelli, O., Bonaccini, D., Close, L., Currie, D., & Parmeggiani, G. 2000, *A&AS*, 147, 335
- Dulick, M., Bauschlicher, Jr., C. W., Burrows, A., Sharp, C. M., Ram, R. S., & Bernath, P. 2003, *ApJ*, 594, 651
- Dupuy, T. J., Liu, M. C., & Bowler, B. P. 2009a, *ApJ*, 706, 328
- Dupuy, T. J., Liu, M. C., & Ireland, M. J. 2009b, *ApJ*, 692, 729
- . 2009c, *ApJ*, 699, 168
- Faherty, J. K., Burgasser, A. J., Cruz, K. L., Shara, M. M., Walter, F. M., & Gelino, C. R. 2009, *AJ*, 137, 1
- Forrest, W. J., Shure, M., & Skrutskie, M. F. 1988, *ApJ*, 330, L119
- Forveille, T., et al. 2005, *A&A*, 435, L5
- . 1999, *A&A*, 351, 619
- Gatewood, G., & Coban, L. 2009, *AJ*, 137, 402
- Gautier, III, T. N., et al. 2007, *ApJ*, 667, 527
- Gelino, C. R., Kirkpatrick, J. D., & Burgasser, A. J. 2004, in *Bulletin of the American Astronomical Society*, Vol. 36, *Bulletin of the American Astronomical Society*, 1354
- Ghez, A. M., et al. 2008, *ApJ*, 689, 1044
- Gizis, J. E., Monet, D. G., Reid, I. N., Kirkpatrick, J. D., Liebert, J., & Williams, R. J. 2000, *AJ*, 120, 1085
- Gliese, W., & Jahreiss, H. 1991, in *Nearby Stars, Preliminary 3rd Version (1991)*, 0
- Golimowski, D. A., et al. 2004, *AJ*, 127, 3516
- Grevesse, N., & Noels, A. 1993, in *Origin and Evolution of the Elements*, ed. N. Prantzos, E. Vangioni-Flam, & M. Casse, 15–25
- Helling, C., & Woitke, P. 2006, *A&A*, 455, 325
- Helling, C., Woitke, P., & Thi, W. 2008, *A&A*, 485, 547
- Henry, T. J., & Kirkpatrick, J. D. 1990, *ApJ*, 354, L29
- Johnas, C. M. S., Helling, C., Dehn, M., Woitke, P., & Hauschildt, P. H. 2008, *MNRAS*, 385, L120
- Kirkpatrick, J. D. 2003, in *Proceedings of IAU Symposium 211: Brown Dwarfs*, ed. E. Martin, 189

- Kirkpatrick, J. D., et al. 2008, *ApJ*, 689, 1295
- Kirkpatrick, J. D., McGraw, J. T., Hess, T. R., Liebert, J., & McCarthy, Jr., D. W. 1994, *ApJS*, 94, 749
- Konopacky, Q. M., Ghez, A. M., Barman, T. S., Rice, E. L., Bailey, J. I., White, R. J., McLean, I. S., & Duchêne, G. 2010, *ApJ*, 711, 1087
- Krist, J. 1995, in *Astronomical Society of the Pacific Conference Series*, Vol. 77, *Astronomical Data Analysis Software and Systems IV*, ed. R. A. Shaw, H. E. Payne, & J. J. E. Hayes, 349
- Lane, B. F., Zapatero Osorio, M. R., Britton, M. C., Martín, E. L., & Kulkarni, S. R. 2001, *ApJ*, 560, 390
- Law, N. M., Hodgkin, S. T., & Mackay, C. D. 2008, *MNRAS*, 384, 150
- Leinert, C., Jahreiß, H., Woitas, J., Zucker, S., Mazeh, T., Eckart, A., & Köhler, R. 2001, *A&A*, 367, 183
- Lenzen, R., et al. 2003, *Proc. SPIE*, 4841, 944
- Lépine, S., Thorstensen, J. R., Shara, M. M., & Rich, R. M. 2009, *AJ*, 137, 4109
- Liu, M. C., Dupuy, T. J., & Ireland, M. J. 2008, *ApJ*, 689, 436
- Luhman, K. L., Stauffer, J. R., & Mamajek, E. E. 2005, *ApJ*, 628, L69
- Markwardt, C. B. 2009, in *Astronomical Society of the Pacific Conference Series*, Vol. 411, *Astronomical Society of the Pacific Conference Series*, ed. D. A. Bohlender, D. Durand, & P. Dowler, 251
- Martín, E. L., Brandner, W., Bouy, H., Basri, G., Davis, J., Deshpande, R., & Montgomery, M. M. 2006, *A&A*, 456, 253
- Martín, E. L., Koresko, C. D., Kulkarni, S. R., Lane, B. F., & Wizinowich, P. L. 2000, *ApJ*, 529, L37
- McGovern, M. R., Kirkpatrick, J. D., McLean, I. S., Burgasser, A. J., Prato, L., & Lowrance, P. J. 2004, *ApJ*, 600, 1020
- Mohanty, S., Basri, G., Jayawardhana, R., Allard, F., Hauschildt, P., & Ardila, D. 2004, *ApJ*, 609, 854
- Montagnier, G., et al. 2006, *A&A*, 460, L19
- Osten, R. A., Phan-Bao, N., Hawley, S. L., Reid, I. N., & Ojha, R. 2009, *ApJ*, 700, 1750
- Partridge, H., & Schwenke, D. W. 1997, *J. Chem. Phys.*, 106, 4618

- Perryman, M. A. C., & ESA, eds. 1997, ESA Special Publication, Vol. 1200, The HIPPARCOS and TYCHO catalogues. Astrometric and photometric star catalogues derived from the ESA HIPPARCOS Space Astrometry Mission
- Phan-Bao, N., Osten, R. A., Lim, J., Martín, E. L., & Ho, P. T. P. 2007, *ApJ*, 658, 553
- Phillips, J. G., & Davis, S. P. 1993, *ApJ*, 409, 860
- Pozio, F. 1991, *Memorie della Societa Astronomica Italiana*, 62, 171
- Preibisch, T., & Feigelson, E. D. 2005, *ApJS*, 160, 390
- Rayner, J. T., Cushing, M. C., & Vacca, W. D. 2009, *ApJS*, 185, 289
- Rayner, J. T., Toomey, D. W., Onaka, P. M., Denault, A. J., Stahlberger, W. E., Vacca, W. D., Cushing, M. C., & Wang, S. 2003, *PASP*, 115, 362
- Rebolo, R., Martín, E. L., & Magazzu, A. 1992, *ApJ*, 389, L83
- Reid, I. N., Burgasser, A. J., Cruz, K. L., Kirkpatrick, J. D., & Gizis, J. E. 2001, *AJ*, 121, 1710
- Reid, I. N., et al. 2003, *AJ*, 126, 3007
- Reiners, A., & Basri, G. 2009, *ApJ*, 705, 1416
- Reiners, A., & Basri, G. 2010, *ApJ*, 710, 924
- Reiners, A., Homeier, D., Hauschildt, P. H., & Allard, F. 2007, *A&A*, 473, 245
- Rice, E. L., Barman, T., Mclean, I. S., Prato, L., & Kirkpatrick, J. D. 2010, *ApJS*, 186, 63
- Robin, A. C., Reylé, C., Derrière, S., & Picaud, S. 2003, *A&A*, 409, 523
- Rousset, G., et al. 2003, *Proc. SPIE*, 4839, 140
- Saumon, D., & Marley, M. S. 2008, *ApJ*, 689, 1327
- Schmitt, J. H. M. M., Fleming, T. A., & Giampapa, M. S. 1995, *ApJ*, 450, 392
- Schwenke, D. W. 1998, *Chemistry and Physics of Molecules and Grains in Space. Faraday Discussions No. 109. The Faraday Division of the Royal Society of Chemistry, London, 1998., p.321, 109, 321*
- Seifahrt, A., Röhl, T., Neuhäuser, R., Reiners, A., Kerber, F., Käuffl, H. U., Siebenmorgen, R., & Smette, A. 2008, *A&A*, 484, 429
- Simon, M., Bender, C., & Prato, L. 2006, *ApJ*, 644, 1183
- Simons, D. A., & Tokunaga, A. 2002, *PASP*, 114, 169

- Soderblom, D. R., Pilachowski, C. A., Fedele, S. B., & Jones, B. F. 1993, *AJ*, 105, 2299
- Stauffer, J. R., Schultz, G., & Kirkpatrick, J. D. 1998, *ApJ*, 499, L199
- Tokunaga, A. T., Simons, D. A., & Vacca, W. D. 2002, *PASP*, 114, 180
- Torres, C. A. O., Quast, G. R., Melo, C. H. F., & Sterzik, M. F. 2008, *Young Nearby Loose Associations*, ed. Reipurth, B., 757
- Vacca, W. D., Cushing, M. C., & Rayner, J. T. 2003, *PASP*, 115, 389
- van Biesbroeck, G. 1944, *AJ*, 51, 61
- van Dam, M. A., Le Mignant, D., & Macintosh, B. A. 2004, *Appl. Opt.*, 43, 5458
- van Dam, M. A., et al. 2006, *PASP*, 118, 310
- van Leeuwen, F. 2007, *Hipparcos, the New Reduction of the Raw Data (Hipparcos, the New Reduction of the Raw Data. By Floor van Leeuwen, Institute of Astronomy, Cambridge University, Cambridge, UK Series: Astrophysics and Space Science Library, Vol. 350 20 Springer Dordrecht)*
- Wallace, L., & Hinkle, K. 2001, *ApJ*, 559, 424
- Walsh, J. R., Goudfrooij, P., & Malumuth, E. 2001, *STIS Geometric Distortion: SMOV3A tests for CCD, NUV-MAMA and FUV-MAMA*, Tech. rep.
- West, A. A., Hawley, S. L., Bochanski, J. J., Covey, K. R., Reid, I. N., Dhital, S., Hilton, E. J., & Masuda, M. 2008, *AJ*, 135, 785
- Witte, S., Helling, C., & Hauschildt, P. H. 2009, *A&A*, 506, 1367
- Wizinowich, P., et al. 2000, *PASP*, 112, 315
- Wizinowich, P. L., et al. 2006, *PASP*, 118, 297
- Woitke, P., & Helling, C. 2003, *A&A*, 399, 297
- Zapatero Osorio, M. R., Lane, B. F., Pavlenko, Y., Martín, E. L., Britton, M., & Kulkarni, S. R. 2004, *ApJ*, 615, 958
- Zuckerman, B., & Song, I. 2004, *ARA&A*, 42, 685

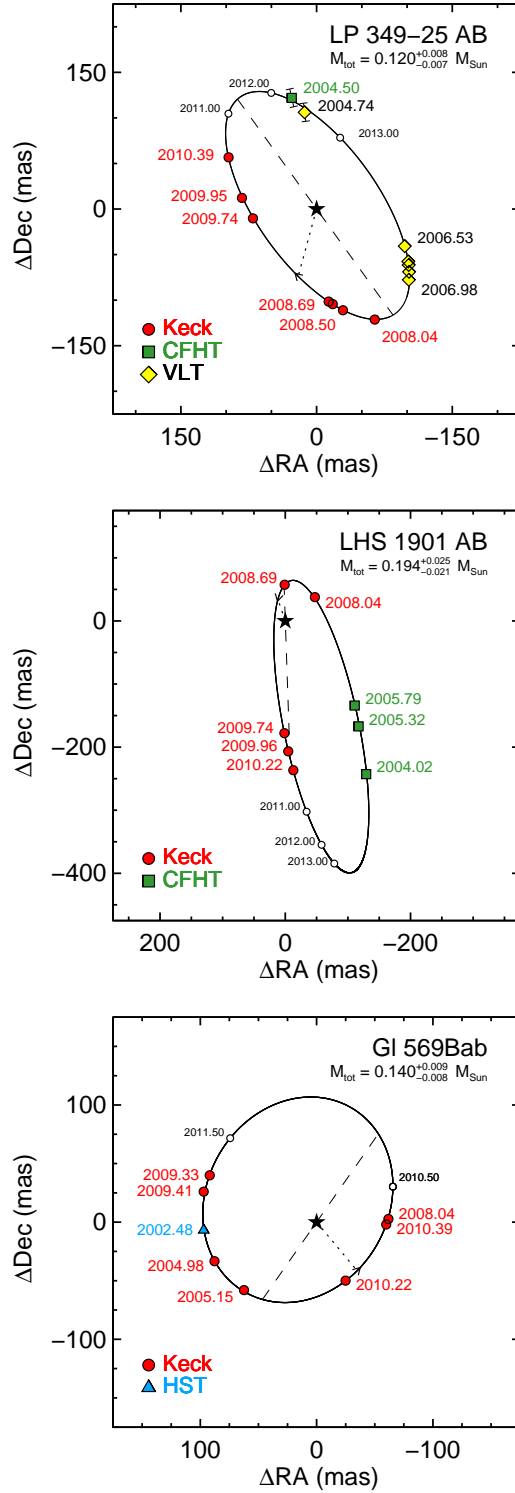


Fig. 1.— Relative astrometry for LP 349-25AB, LHS 1901AB, and GI 569Bab along with the best-fitting orbits. The dotted line and arrow indicate the time of periastron passage, the dashed line shows the line of nodes, and the empty circles show predicted future locations. Error bars are typically smaller than the plotting symbols. All orbits are sufficiently well constrained that the uncertainties in the total masses are dominated by the parallax errors.

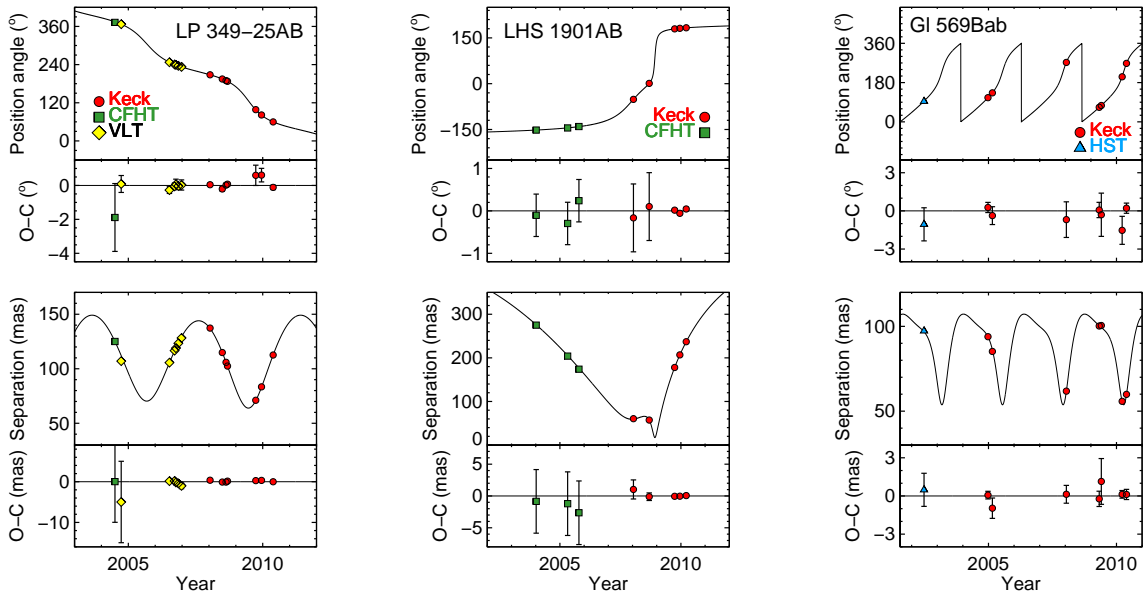


Fig. 2.— Measurements of the projected separation and PA of LP 349-25AB (*left*), LHS 1901AB (*middle*), and Gl 569Bab (*right*). The best-fit orbits from our MCMC analysis are shown as solid lines. The bottom panel of each plot shows the observed minus computed ($O - C$) measurements with observational error bars.

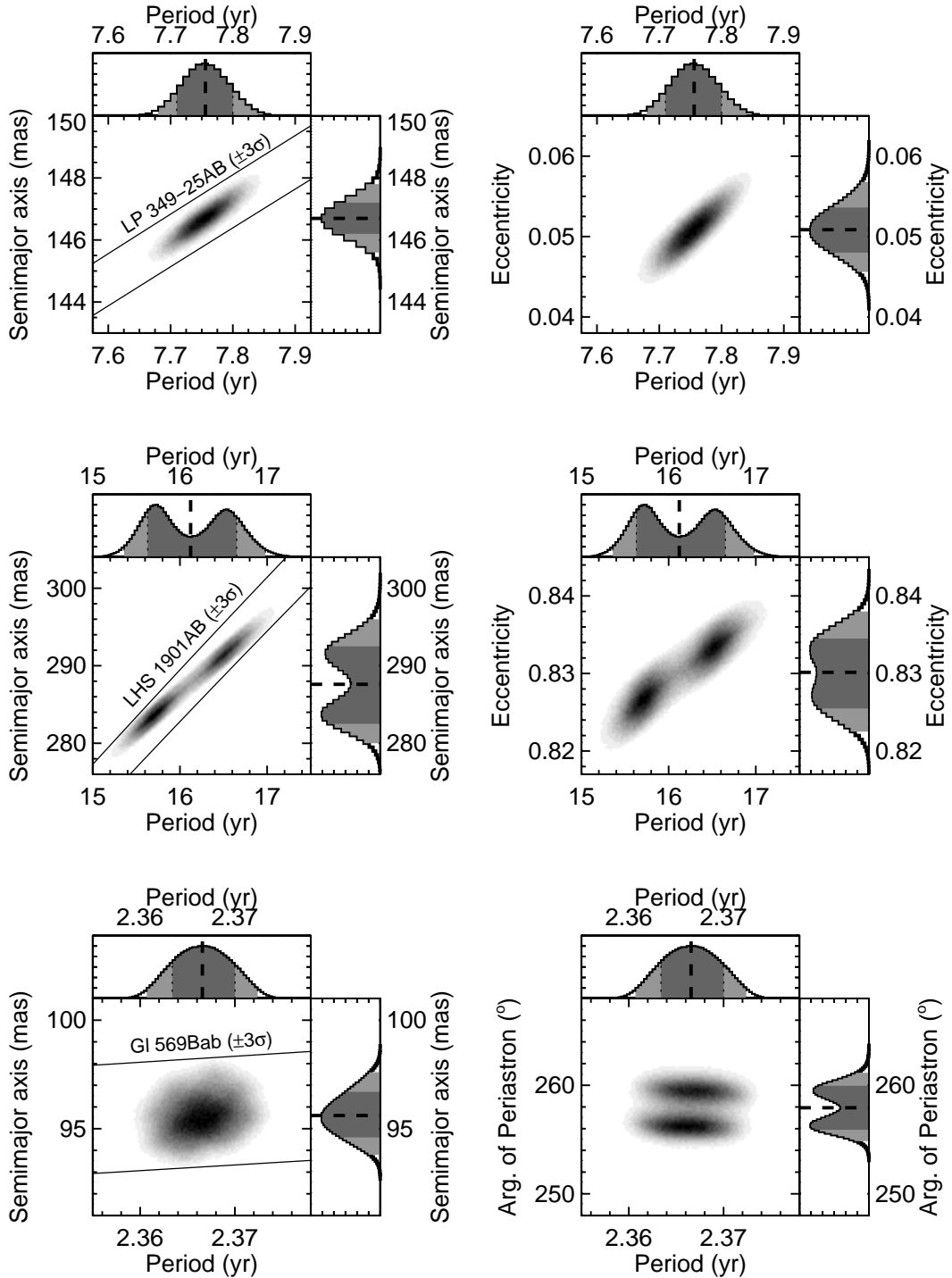


Fig. 3.— The covariance between the orbital parameters for LP 349-25AB (*top*), LHS 1901AB (*middle*), and Gl 569Bab (*bottom*) shown in grayscale using all 2×10^6 saved steps from our MCMC chains of length 2×10^8 . For LP 349-25AB and LHS 1901AB the correlation between P and a enables the total mass to be determined more precisely than from simple propagation of errors, as illustrated by lines drawn demarcating the 3σ range for the total mass (prior accounting for the distance uncertainty). The double-peaked nature of the MCMC parameter distributions for LHS 1901AB and Gl 569Bab also reveal slightly degenerate orbit solutions.

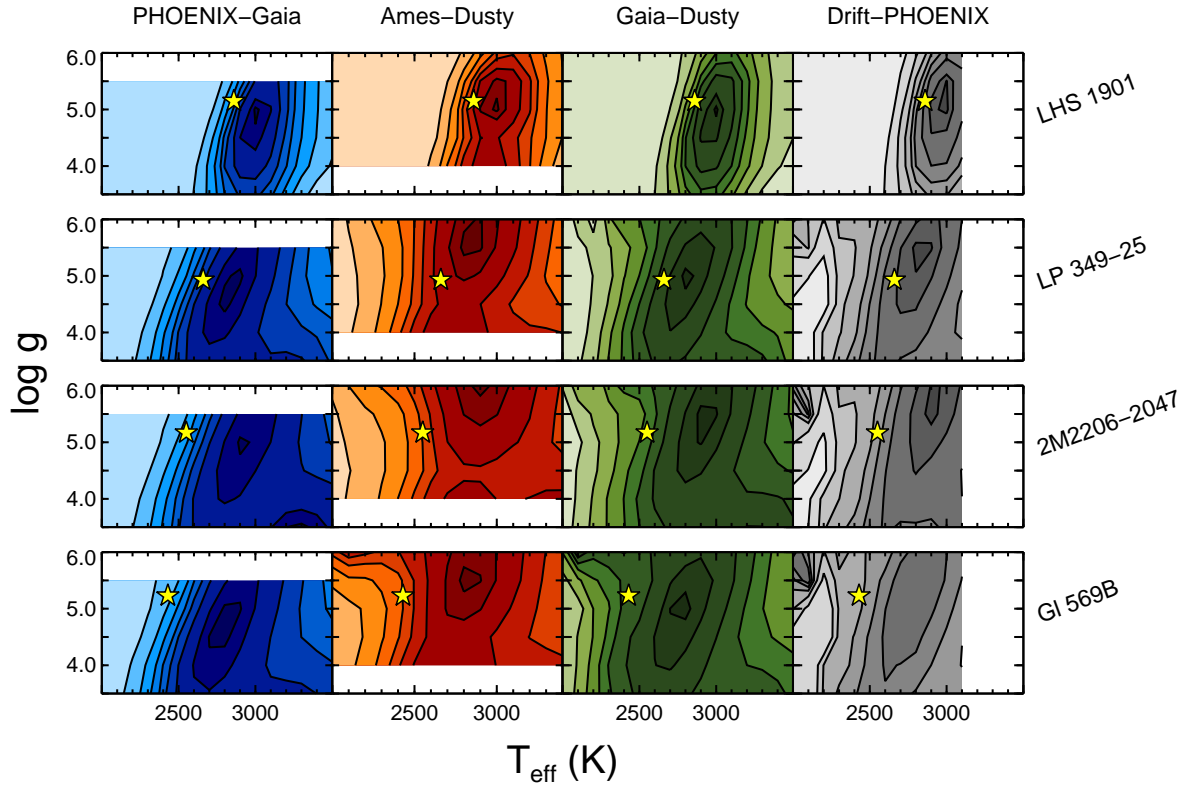


Fig. 4.— Contours of the χ^2 values from model atmosphere fits to our sample binaries’ observed integrated-light 0.95–2.42 μm spectra (drawn at 1.02, 1.1, 1.3, 1.5, 1.7, 2.0, 2.5, and 3.5 times the minimum χ^2). T_{eff} is generally better constrained than $\log(g)$, as indicated by contours that are elongated in the $\log(g)$ direction. White space shows where models are not present in our grids. For comparison, the gold stars show Lyon Dusty evolutionary model-derived properties, with $\log(g)$ in general agreement but T_{eff} systematically lower than the best-fit model atmospheres (see Section 4.3).

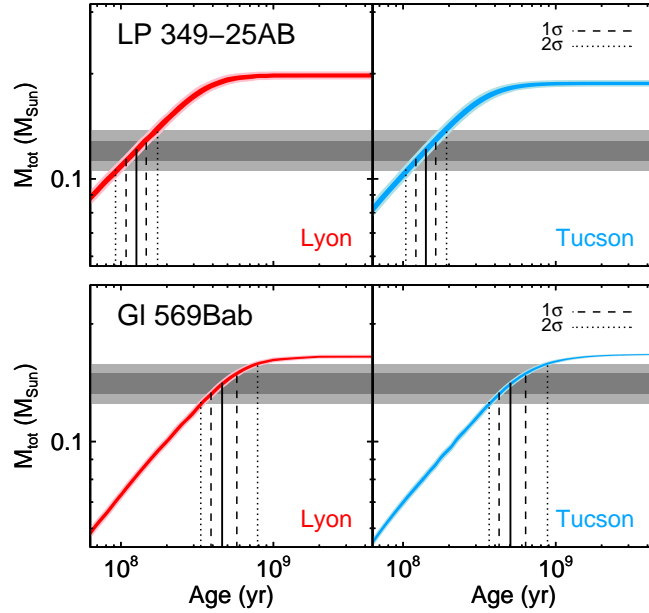


Fig. 5.— Total mass (M_{tot}) of LP 349-25AB and Gl 569Bab predicted by evolutionary models as a function of age, given the observational constraint of the luminosities of the individual components. The curved shaded regions show the 1σ and 2σ ranges in the model-derived masses, which increase as a function of age. By applying the independent constraint of the measured total masses, we used Lyon models (left panel) and Tucson models (right panel) to derive ages for these binaries (see Tables 7 and 9). The horizontal gray bars show our 1σ and 2σ constraints on the total mass, and the resulting median, 1σ , and 2σ model-inferred ages are shown by solid, dashed, and dotted lines, respectively. Because LP 349-25AB has a lower mass than Gl 569Bab (and higher luminosities), its derived age is significantly younger than for Gl 569Bab.

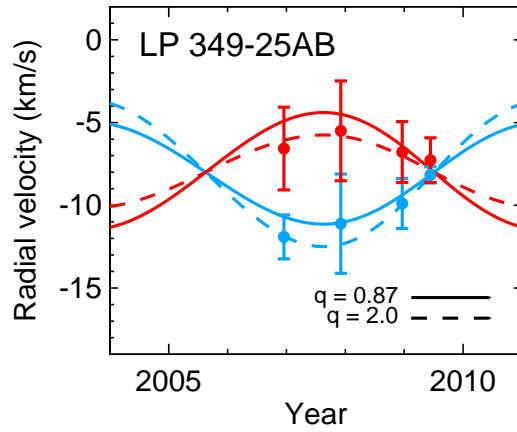


Fig. 6.— Radial velocities of LP 349-25A (blue) and LP 349-25B (red) as measured by Konopacky et al. (2010) shown with curves predicted by our best-fit orbit, assuming two different mass ratios ($q \equiv M_2/M_1$). Combining our measured luminosity ratio and total mass, evolutionary models predict $q = 0.87$, whereas Konopacky et al. (2010) found $q = 2.0$ from the best fit to their data. Their $1\text{--}3 \text{ km s}^{-1}$ errors result in an unrealistically low χ^2 (0.5 for 6 DOF), suggesting that the errors are overestimated. Within these large errors, we find that both mass ratios are allowed by their data.

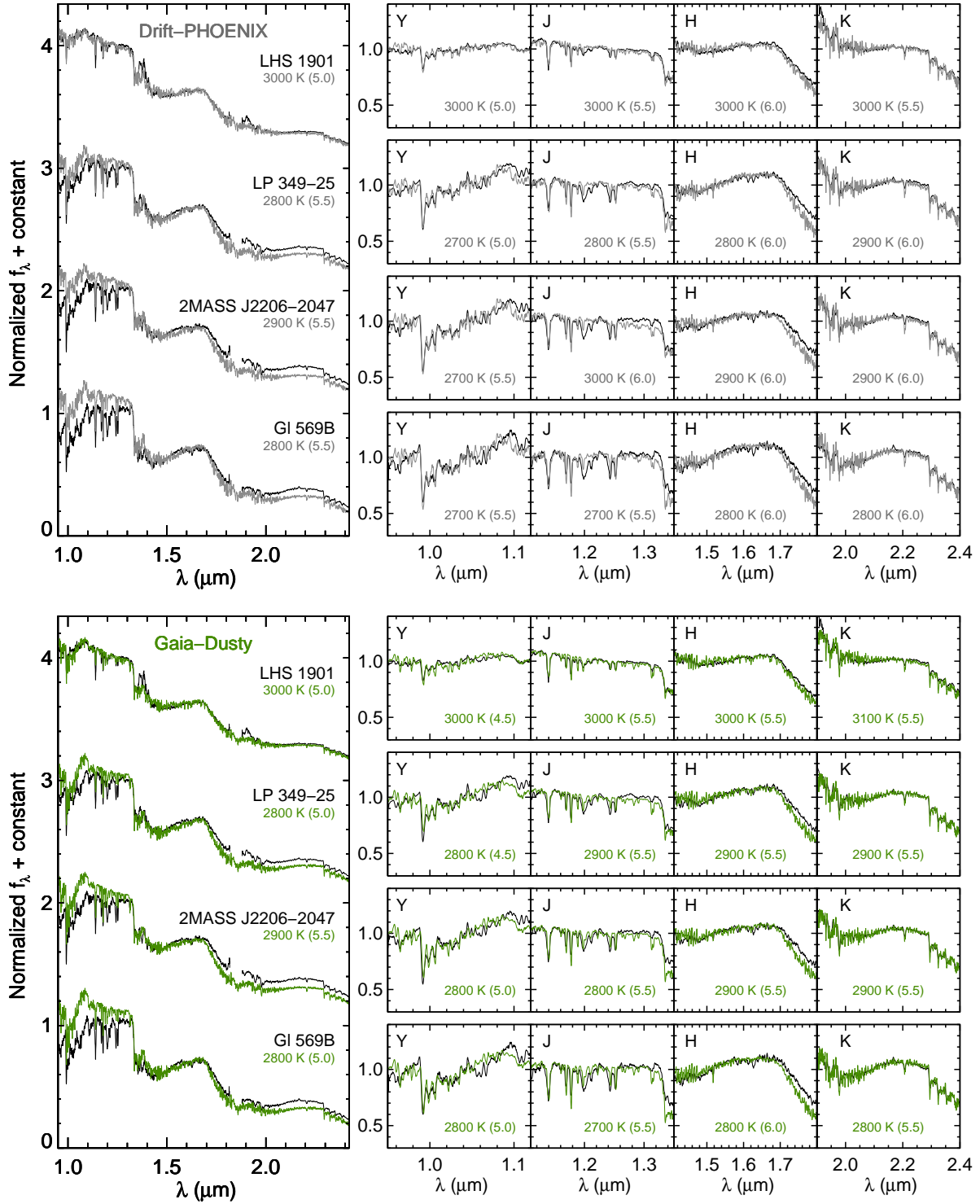


Fig. 7.— Integrated-light SpeX SXD spectra (black) shown with the *best fitting atmospheric model spectra* (top: Drift-PHOENIX, gray; bottom: Gaia-Dusty, green). Each best-fit model spectrum is labeled indicating its effective temperature, with surface gravity in parentheses. We performed separate fits for the full NIR SED (left) and individual bands (right). All spectra are smoothed by 10 pixels $\approx 0.003 \mu\text{m}$ for display only.

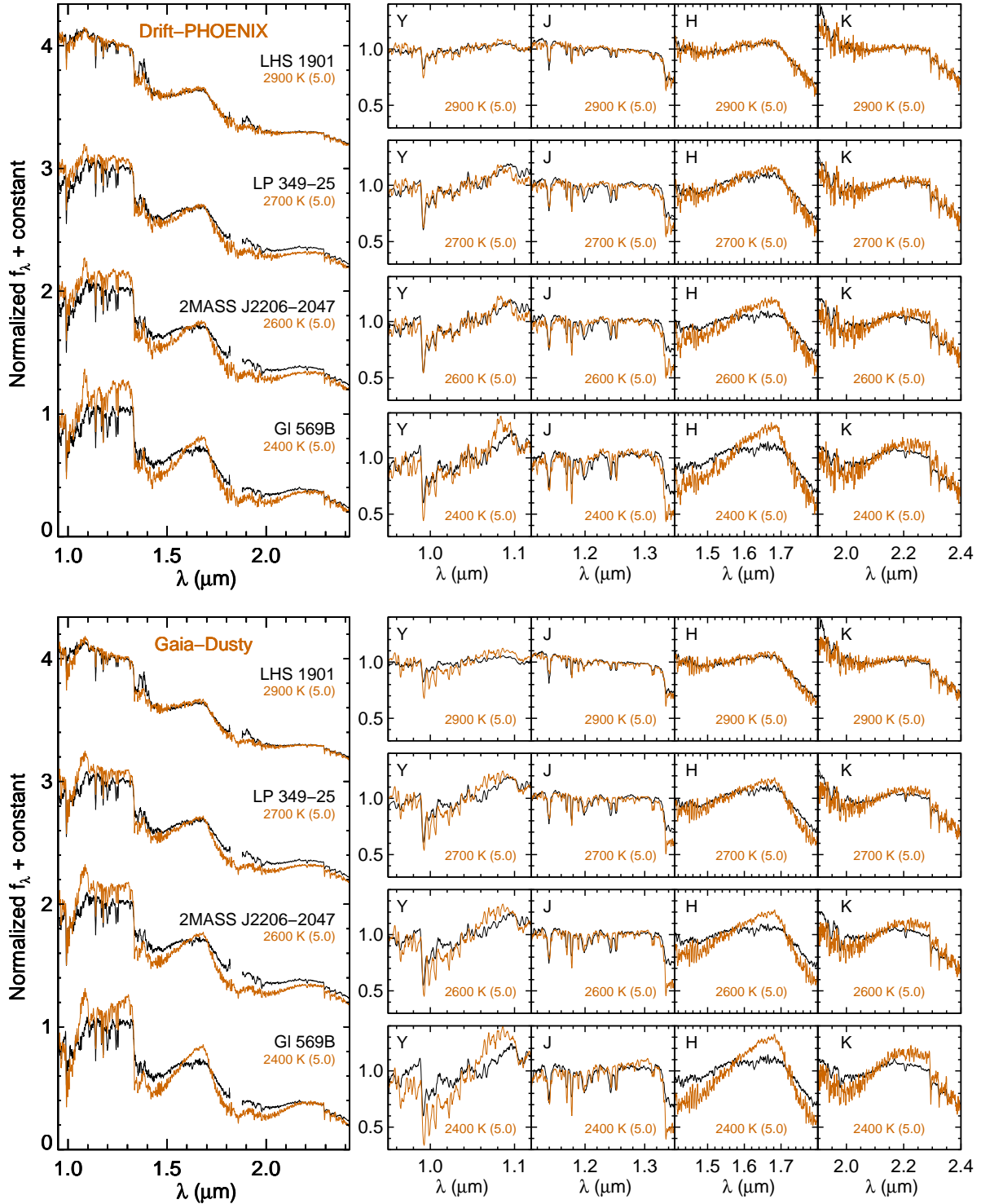


Fig. 8.— Integrated-light SpeX SXD spectra (black) shown with the *atmospheric model spectra* corresponding to the values of T_{eff} and $\log(g)$ derived from *Lyon Dusty* evolutionary models. Each model spectrum (brown) is labeled indicating its effective temperature, with surface gravity in parentheses. All spectra are smoothed by 10 pixels $\approx 0.003 \mu\text{m}$ for display only. The most prominent deviations in the model spectra are: the exaggerated shapes of *H* and *K* bands; the overpredicted depth of H_2O absorption at $1.33 \mu\text{m}$; and the strength of the FeH bandhead at $0.99 \mu\text{m}$. Without directly measured radii we cannot determine if the problem lies in the model spectra, the evolutionary model radii, or both.

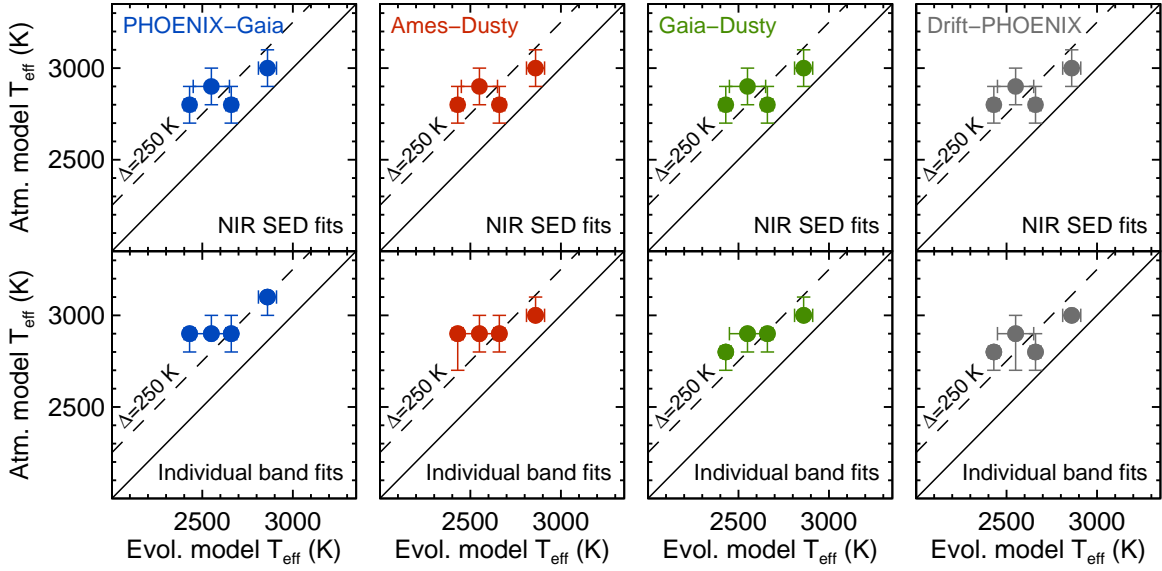


Fig. 9.— Effective temperatures determined from model atmosphere fitting compared to Lyon Dusty evolutionary model-derived T_{eff} (i.e., from measured total mass and individual luminosities). Results from fitting NIR SEDs (top; 100 K error bars) are shown separately from the results of fitting individual bandpass (bottom; error bars indicate full range of band fits). Measurements typically lie above (or to the left of) the line of equality. An offset of 250 K can largely account for the observed discrepancies (dashed line), implying that either evolutionary model estimates are too cool (i.e., radii too large by 15–20%) or that atmospheric model estimates are too warm by 250 K.

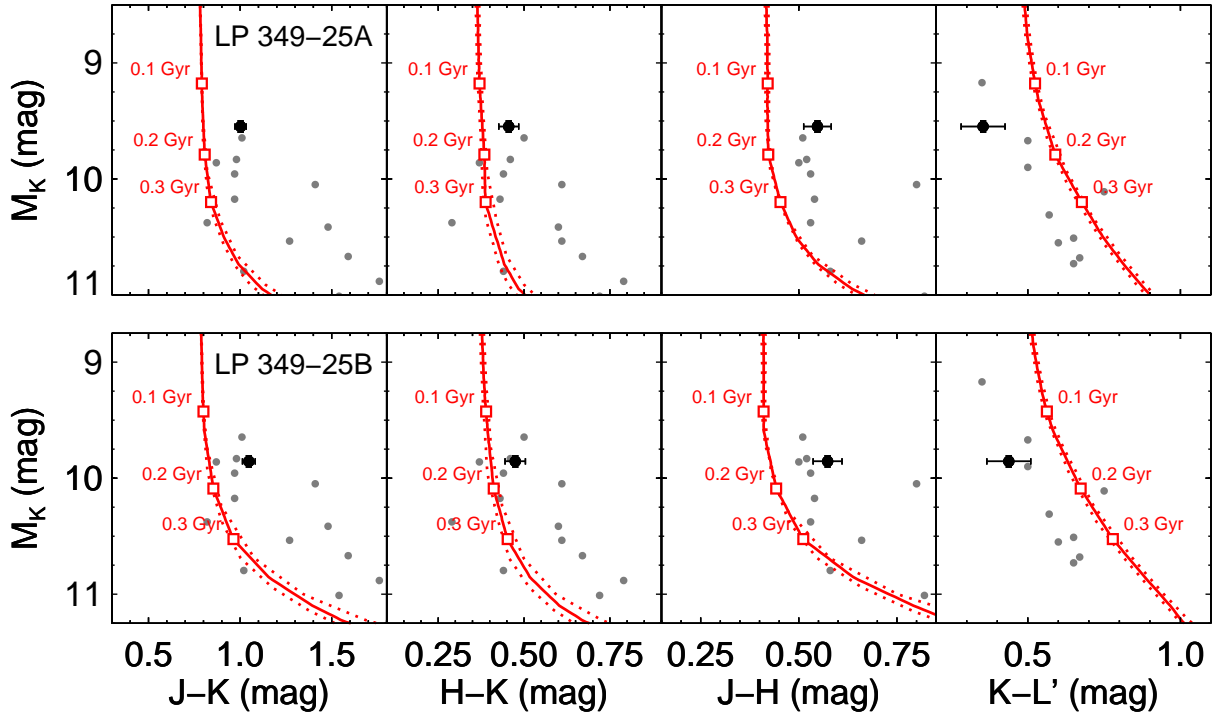


Fig. 10.— Color-magnitude diagrams showing the measured photometry of LP 349-25A (top) and LP 349-25B (bottom) compared to Lyon evolutionary tracks (all photometry on the MKO system). The solid lines are isomass tracks from the Dusty (Chabrier et al. 2000) models with dotted lines encompassing the 1σ mass uncertainties, and open squares demarcate ages of 0.1, 0.2, and 0.3 Gyr. Field dwarfs with parallax measurements are shown for comparison as filled gray circles. LP 349-25A and B are somewhat redder (0.1–0.2 mag) than evolutionary model tracks for JHK colors, while their $K - L'$ colors are 0.1–0.2 mag bluer than models.

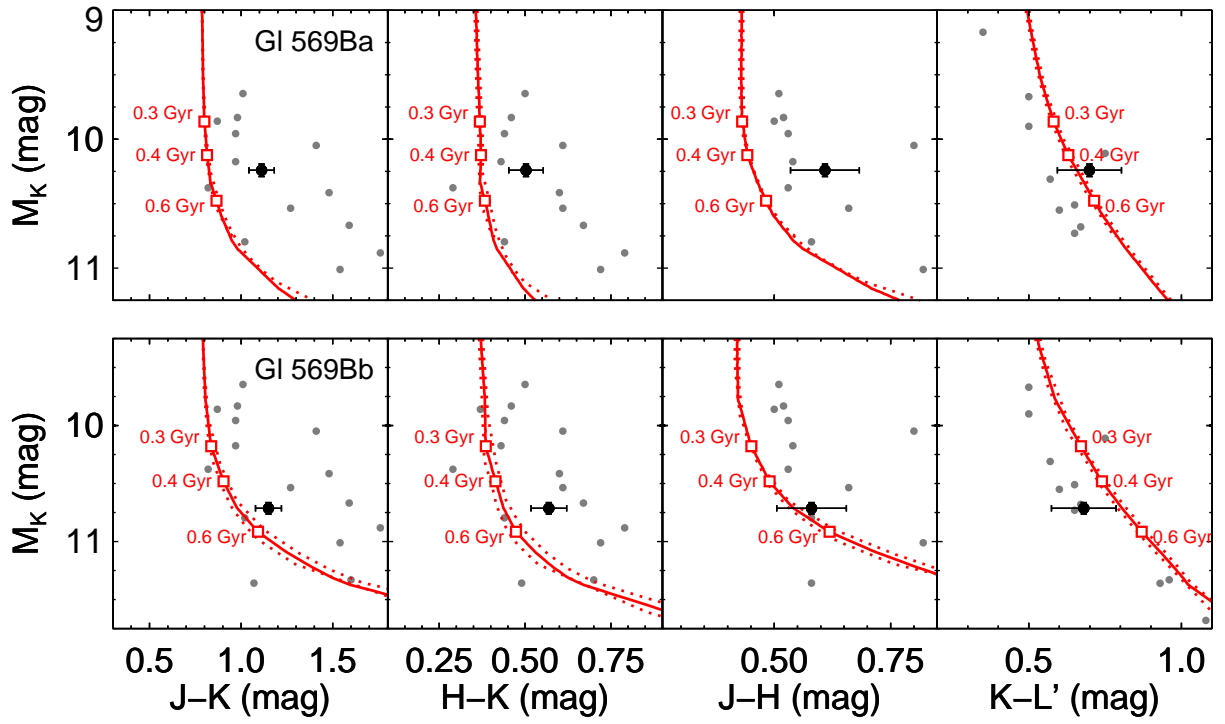


Fig. 11.— Same as Figure 10 but for Gl 569Bab.

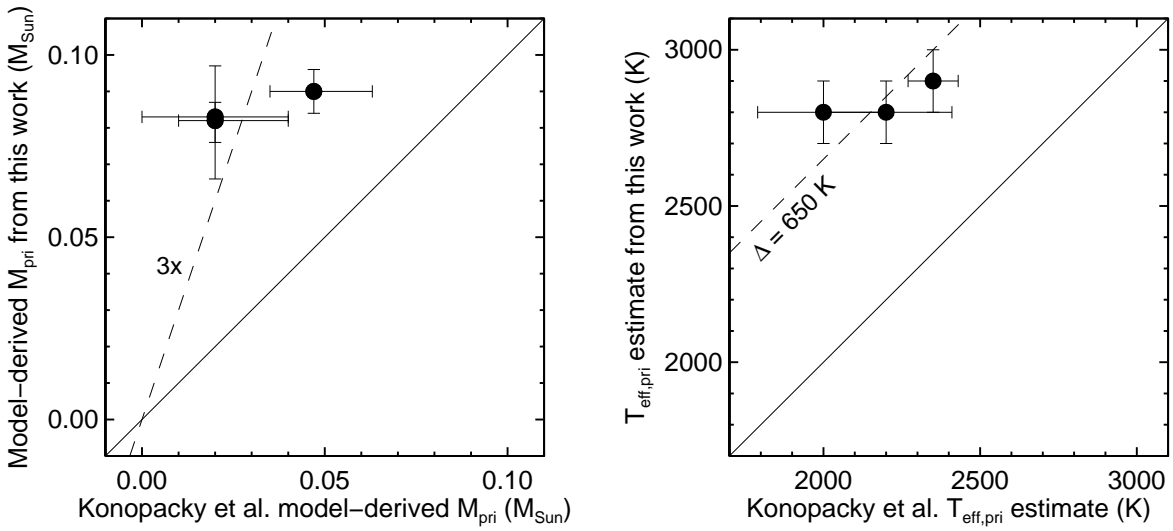


Fig. 12.— Comparison of the primary component masses derived from evolutionary models using the $L_{\text{bol}}-T_{\text{eff}}$ approach by Konopacky et al. (2010) and by us. The masses we derive using this approach are systematically higher by a factor of ~ 2 to 4 (left) because our model atmosphere fitting of integrated-light spectra yielded ≈ 650 K higher temperatures than their fitting of resolved broadband photometry (right). We suggest that the sensitivity of this model testing approach to the input T_{eff} estimates makes it more likely to identify problems with model atmospheres than evolutionary models.

Table 1. Keck AO Observations

Date (UT)	Time (UT)	Airmass	Filter	FWHM ^a (mas)	Strehl ratio ^a
LP 349-25AB					
2008 Jan 16 ^c	05:56	1.280	K_S	57 ± 3	0.23 ± 0.05
2008 Jun 30 ^c	13:20	1.314	J	55 ± 4	0.026 ± 0.009
	13:29	1.274	H	48.6 ± 0.8	0.123 ± 0.012
2008 Aug 20 ^b	13:12	1.350	K_S	58 ± 4	0.19 ± 0.04
	14:21	1.069	K_S	50.1 ± 0.5	0.448 ± 0.007
2008 Sep 9 ^b	13:51	1.169	L'	80.2 ± 0.9	0.78 ± 0.03
2009 Sep 28 ^c	13:17	1.328	K_S	54 ± 3	0.29 ± 0.05
2009 Dec 15 ^c	05:22	1.479	K	55.8 ± 0.9	0.33 ± 0.03
2010 May 22 ^c	14:54	1.721	K	58 ± 3	0.36 ± 0.04
LHS 1901AB					
2008 Jan 15 ^b	11:05	1.128	K_S	49.0 ± 1.9	0.411 ± 0.012
2008 Sep 9 ^b	15:13	1.411	J	39.8 ± 1.8	0.087 ± 0.015
	14:59	1.475	H	42.6 ± 1.3	0.217 ± 0.014
	15:17	1.393	K_S	46.7 ± 1.1	0.47 ± 0.03
2009 Sep 28 ^b	15:37	1.150	K_S	51 ± 3	0.30 ± 0.07
2009 Dec 16 ^b	08:45	1.428	K_S	53.7 ± 1.7	0.30 ± 0.04
2010 Mar 22 ^b	05:59	1.096	J	41 ± 5	0.05 ± 0.02
	05:55	1.094	H	40.1 ± 0.8	0.23 ± 0.03
	05:52	1.093	K	50.3 ± 0.2	0.43 ± 0.02
	06:04	1.097	L'	82.7 ± 0.4	0.63 ± 0.07
G1 569Bab					
2004 Dec 24 ^{b,d}	16:22	1.270	H	46.8 ± 0.5	0.17 ± 0.04
2005 Feb 25 ^{b,d}	12:08	1.298	H_{cont}	39.0 ± 1.1	0.23 ± 0.03
2008 Jan 16 ^b	16:33	1.036	H_{cont}	36.9 ± 0.8	0.31 ± 0.05
2009 Apr 29 ^b	12:24	1.089	K_{cont}	50.0 ± 1.3	0.39 ± 0.07
2009 May 29 ^b	10:56	1.159	K_{cont}	52.0 ± 0.7	0.58 ± 0.04
2010 Mar 22 ^b	15:48	1.235	K	48.6 ± 1.2	0.50 ± 0.06
2010 May 23 ^b	11:10	1.133	J	37 ± 2	0.067 ± 0.011
	11:16	1.148	H	40.6 ± 1.6	0.19 ± 0.06
	11:23	1.166	K	49.8 ± 0.6	0.44 ± 0.04
	11:32	1.193	L'	82.4 ± 0.5	0.76 ± 0.02

^aStrehl ratios and FWHM were computed using the publicly available routine NIRC2STREHL. Errors are the rms of individual dithers.

^bNGS AO observations.

^cLGS AO observations.

^dData originally published by Simon et al. (2006) and reanalyzed by us.

Table 2. Best-Fit Binary Parameters

Epoch (UT)	Instrument	Filter	ρ (mas)	PA ($^\circ$)	Δm (mag)
LP 349-25AB					
2004 Jul 3	CFHT/PUEO ^{a,b}	K'	125 ± 10	12.7 ± 2.0	0.26 ± 0.05
2004 Sep 26	VLT/NACO ^{a,b}	H	107 ± 10	7.1 ± 0.5	0.38 ± 0.05
2006 Jul 13	VLT/NACO ^a	K_S	105.6 ± 0.3	247.3 ± 0.2	0.33 ± 0.03
2006 Sep 21	VLT/NACO ^a	K_S	116.6 ± 0.6	240.4 ± 0.2	0.31 ± 0.03
2006 Oct 9	VLT/NACO ^a	K_S	118.9 ± 0.6	238.9 ± 0.3	0.285 ± 0.013
2006 Nov 11	VLT/NACO ^a	K_S	123.3 ± 0.4	236.0 ± 0.2	0.315 ± 0.019
2006 Dec 24	VLT/NACO ^a	K_S	128.2 ± 0.7	232.7 ± 0.3	0.276 ± 0.018
2008 Jan 16	Keck/NIRC2 ^a	K_S	137.3 ± 0.4	207.92 ± 0.09	0.315 ± 0.011
2008 Jun 30	Keck/NIRC2	J	115.2 ± 0.3	194.4 ± 0.4	0.35 ± 0.03
	Keck/NIRC2 ^a	H	114.87 ± 0.12	194.71 ± 0.13	0.326 ± 0.011
	Keck/NIRC2	K_S	115.2 ± 0.5	194.64 ± 0.13	0.318 ± 0.007
2008 Aug 20	Keck/NIRC2 ^a	K_S	105.9 ± 0.2	189.71 ± 0.11	0.314 ± 0.007
2008 Sep 9	Keck/NIRC2 ^a	L'	102.45 ± 0.19	187.46 ± 0.10	0.222 ± 0.005
2008 Sep 28	Keck/NIRC2 ^a	K_S	71.1 ± 0.3	98.3 ± 0.6	0.24 ± 0.03
2009 Dec 15	Keck/NIRC2 ^a	K	83.4 ± 0.3	81.6 ± 0.4	0.38 ± 0.06
2010 May 22	Keck/NIRC2 ^a	K	112.6 ± 0.4	59.76 ± 0.13	0.307 ± 0.008
LHS 1901AB					
2004 Jan 8	CFHT/PUEO ^{a,c}	K'	275 ± 5	208.0 ± 0.5	0.13 ± 0.03
2005 Apr 27	CFHT/PUEO ^{a,c}	K'	204 ± 5	215.0 ± 0.5	0.07 ± 0.03
2005 Oct 14	CFHT/PUEO ^{a,c}	H	174 ± 5	219.6 ± 0.5	0.14 ± 0.05
2008 Jan 15	Keck/NIRC2 ^a	K_S	60.5 ± 1.5	308.6 ± 0.8	0.16 ± 0.06
2008 Sep 9	Keck/NIRC2 ^a	J	57.4 ± 0.6	1.0 ± 0.8	0.31 ± 0.16
	Keck/NIRC2	H	57.2 ± 1.3	1.2 ± 1.8	0.28 ± 0.13
	Keck/NIRC2	K_S	57.8 ± 1.0	1.5 ± 0.8	0.15 ± 0.04
2009 Sep 28	Keck/NIRC2 ^a	K_S	177.90 ± 0.14	179.54 ± 0.03	0.098 ± 0.007
2009 Dec 16	Keck/NIRC2 ^a	K_S	206.78 ± 0.13	181.31 ± 0.03	0.094 ± 0.003
2010 Mar 22	Keck/NIRC2	J	236.9 ± 0.4	183.12 ± 0.03	0.111 ± 0.016
	Keck/NIRC2	H	236.9 ± 0.4	183.11 ± 0.04	0.115 ± 0.009
	Keck/NIRC2 ^a	K	237.0 ± 0.3	183.10 ± 0.04	0.107 ± 0.007
	Keck/NIRC2	L'	237.3 ± 0.7	183.15 ± 0.05	0.099 ± 0.003
G1 569Bab					
2002 Jun 26	<i>HST</i> /STIS ^a	F28X50LP	97.3 ± 1.3	94.0 ± 1.3	0.99 ± 0.03
2004 Dec 24	Keck/NIRC2 ^a	H	93.9 ± 0.3	110.8 ± 0.4	0.54 ± 0.02
2005 Feb 25	Keck/NIRC2 ^a	H_{cont}	85.2 ± 0.8	132.9 ± 0.7	0.55 ± 0.08
2008 Jan 16	Keck/NIRC2 ^a	H_{cont}	61.8 ± 0.7	272.5 ± 1.4	0.58 ± 0.16
2009 Apr 29	Keck/NIRC2 ^a	K_{cont}	100.2 ± 0.6	66.5 ± 0.6	0.55 ± 0.07
2009 May 29	Keck/NIRC2 ^a	K_{cont}	100.5 ± 1.8	75.0 ± 1.7	0.59 ± 0.07
2010 Mar 22	Keck/NIRC2 ^a	K	55.8 ± 0.3	206.5 ± 1.1	0.473 ± 0.010
2010 May 23	Keck/NIRC2	J	58.5 ± 1.1	265.9 ± 1.0	0.45 ± 0.13
	Keck/NIRC2	H	58.8 ± 0.5	267.6 ± 0.6	0.46 ± 0.06
	Keck/NIRC2 ^a	K	59.9 ± 0.4	268.1 ± 0.4	0.49 ± 0.04
	Keck/NIRC2	L'	59.9 ± 0.6	267.6 ± 0.5	0.49 ± 0.03

^aUsed in the orbit fit.

^bMeasurements from Forveille et al. (2005).

^cMeasurements from Montagnier et al. (2006).

Table 3. Derived Orbital Parameters^a

Parameter	MCMC			MPFIT routine
	Median	68.3% c.l.	95.4% c.l.	
LP 349-25AB				
Semimajor axis a (mas)	146.7	–0.6, 0.6	–1.1, 1.2	146.7 ± 0.6
Orbital period P (yr)	7.76	–0.04, 0.04	–0.07, 0.08	7.76 ± 0.04
Eccentricity e	0.051	–0.003, 0.003	–0.005, 0.006	0.051 ± 0.003
Inclination i ($^\circ$)	117.24	–0.14, 0.14	–0.3, 0.3	117.23 ± 0.13
Time of periastron passage $T_0 - 2454860.5^b$ (JD)	0	–24, 26	–50, 50	-2 ± 25
PA of the ascending node Ω ($^\circ$)	35.95	–0.12, 0.12	–0.23, 0.23	35.95 ± 0.11
Argument of periastron ω ($^\circ$)	250	–3, 4	–6, 7	250 ± 3
Total mass (M_\odot): fitted ^c	0.1205	–0.0007, 0.0007	–0.0013, 0.0013	0.1205 ± 0.0006
Total mass (M_\odot): final ^d	0.120	–0.007, 0.008	–0.014, 0.017	0.120 ± 0.008
χ^2 (21 degrees of freedom)	18.1
LHS 1901AB				
Semimajor axis a (mas)	288	–5, 5	–8, 8	288 ± 3
Orbital period P (yr)	16.1	–0.5, 0.5	–0.8, 0.8	16.1 ± 0.3
Eccentricity e	0.830	–0.005, 0.005	–0.008, 0.008	0.830 ± 0.003
Inclination ^a i ($^\circ$)	72.1	–0.3, 0.3	–0.5, 0.5	72.12 ± 0.18
Time of periastron passage $T_0 - 2454765.0^e$ (JD)	0.0	–2.5, 2.5	–4, 4	0.0 ± 1.6
PA of the ascending node Ω ($^\circ$)	182.0	–0.2, 0.2	–0.4, 0.4	181.99 ± 0.15
Argument of periastron ω ($^\circ$)	224.8	–0.6, 0.6	–1.1, 1.1	224.8 ± 0.4
Total mass (M_\odot): fitted ^c	0.1944	–0.0028, 0.0028	–0.005, 0.005	0.1944 ± 0.0018
Total mass (M_\odot): final ^d	0.194	–0.021, 0.025	–0.039, 0.053	0.194 ± 0.023
χ^2 (9 degrees of freedom)	6.8
G1 569Bab				
Semimajor axis a (mas)	95.6	–1.0, 1.1	–1.8, 2.0	95.7 ± 0.7
Orbital period P (yr)	2.367	–0.003, 0.003	–0.006, 0.006	2.367 ± 0.002
Eccentricity e	0.316	–0.005, 0.005	–0.009, 0.009	0.316 ± 0.003
Inclination ^a i ($^\circ$)	35.0	–1.1, 1.1	–2.2, 2.0	35.1 ± 0.7
Time of periastron passage $T_0 - 2455290.5^f$ (JD)	0.0	–1.5, 1.5	–2.5, 2.5	0.0 ± 0.9
PA of the ascending node Ω ($^\circ$)	324.8	–2.0, 2.0	–3.3, 3.3	324.9 ± 1.2
Argument of periastron ω ($^\circ$)	257.9	–2.0, 2.0	–3.0, 3.3	257.8 ± 1.2
Total mass (M_\odot): fitted ^c	0.140	–0.004, 0.005	–0.007, 0.009	0.1408 ± 0.0028
Total mass (M_\odot): final ^d	0.140	–0.008, 0.009	–0.015, 0.018	0.141 ± 0.008
χ^2 (9 degrees of freedom)	6.3

^aNote that the uncertainties quoted here are “single parameter” errors (i.e., $\Delta\chi^2 = 1$) and thus are only valid when a single parameter is of interest.

^b2009 January 27 00:00:00.0 UT

^cThe “fitted” total mass represents the direct results from fitting the observed orbital motion without accounting for the parallax error.

^dThe “final” total mass includes the additional error in the mass due to the error in the parallax.

^e2008 October 25 12:00:00.0 UT

^f2010 April 4 00:00:00.0 UT

Table 4. Measured Properties of Target Binaries^a

Property	LP 349-25			LHS 1901			Gl 569B		
	A	B	Ref.	A	B	Ref.	Ba	Bb	Ref.
$M_{\text{tot}} (M_{\odot})$	$0.120^{+0.008}_{-0.007}$		1,2	$0.194^{+0.025}_{-0.021}$		1,3	$0.140^{+0.009}_{-0.008}$		1,4
Semimajor axis (AU)	1.94 ± 0.04		1,2	3.70 ± 0.16		1,3	0.923 ± 0.018		1,4
d (pc)	13.2 ± 0.3		2	12.9 ± 0.5		3	9.65 ± 0.16		4
Spectral type	$M7.5 \pm 1.0$	$M8.0^{+1.5}_{-1.0}$	1	$M6.5^{+1.0}_{-0.5}$	$M6.5^{+1.0}_{-0.5}$	1	$M8.5 \pm 0.5$	$M9.0 \pm 0.5$	5,6
J (mag)	11.154 ± 0.025	11.506 ± 0.028	1,7	10.631 ± 0.020	10.743 ± 0.020	1,7	11.27 ± 0.06	11.78 ± 0.06	1
H (mag)	10.606 ± 0.023	10.932 ± 0.023	1,7	10.197 ± 0.016	10.312 ± 0.016	1,7	10.67 ± 0.04	11.21 ± 0.04	1
K (mag)	10.151 ± 0.018	10.458 ± 0.018	1,7	9.796 ± 0.019	9.904 ± 0.019	1,7	10.16 ± 0.03	10.64 ± 0.03	1
L' (mag)	9.80 ± 0.07	10.02 ± 0.07	1,8		9.46 ± 0.10	9.95 ± 0.10	1,9
$J - K$ (mag)	1.00 ± 0.03	1.05 ± 0.03	1,7	0.83 ± 0.03	0.84 ± 0.03	1,7	1.11 ± 0.07	1.15 ± 0.07	1
$H - K$ (mag)	0.46 ± 0.03	0.47 ± 0.03	1,7	0.40 ± 0.02	0.41 ± 0.03	1,7	0.50 ± 0.05	0.57 ± 0.05	1
$J - H$ (mag)	0.55 ± 0.03	0.57 ± 0.04	1,7	0.43 ± 0.03	0.43 ± 0.03	1,7	0.61 ± 0.07	0.58 ± 0.07	1
$K - L'$ (mag)	0.35 ± 0.07	0.44 ± 0.07	1,7,8		0.70 ± 0.10	0.68 ± 0.11	1,9
M_J (mag)	10.55 ± 0.05	10.90 ± 0.05	1,2,7	10.09 ± 0.09	10.20 ± 0.09	1,3,7	11.35 ± 0.07	11.86 ± 0.07	1,4
M_H (mag)	10.01 ± 0.05	10.33 ± 0.05	1,2,7	9.65 ± 0.09	9.77 ± 0.09	1,3,7	10.74 ± 0.06	11.28 ± 0.05	1,4
M_K (mag)	9.55 ± 0.05	9.86 ± 0.05	1,2,7	9.25 ± 0.09	9.36 ± 0.09	1,3,7	10.24 ± 0.05	10.71 ± 0.05	1,4,9
$M_{L'}$ (mag)	9.20 ± 0.08	9.42 ± 0.08	1,2,8		9.54 ± 0.10	10.03 ± 0.11	1,4,9
$\log(L_{\text{bol}}/L_{\odot})$	-3.041 ± 0.024	-3.175 ± 0.026	1	-2.95 ± 0.04	-2.99 ± 0.04	1	-3.424 ± 0.019	-3.623 ± 0.020	1
$\Delta \log(L_{\text{bol}})$	0.133 ± 0.019		1	0.044 ± 0.015		1	0.199 ± 0.016		1

^aAll near-infrared photometry on the MKO system.

References. — (1) This work; (2) Gatewood & Coban (2009); (3) Lépine et al. (2009); (4) van Leeuwen (2007); (5) Henry & Kirkpatrick (1990); (6) Zapatero Osorio et al. (2004); (7) Cutri et al. (2003); (8) Golimowski et al. (2004); (9) Forrest et al. (1988).

Table 5. Description of Model Atmosphere Grids

Grid name	Grid Ref.	Molecular line lists				Element abundance	Dust treatment
		H ₂ O	TiO	FeH	CrH		
PHOENIX-Gaia	BH05	Ames	Ames	DA99	F99	GN93	dust disappears after forming (“Cond”)
Ames-Dusty	A01	Ames	Ames	PD93	F99	GN93	dust stays where it forms (“Dusty”)
Gaia-Dusty	B10	BT06	Ames	D03	B02	A05	dust stays where it forms (“Dusty”)
Drift-PHOENIX	W09	Ames	Ames	B06	B06	GN93	nonequilibrium cloud model (“Drift”)

References. — Ames: Partridge & Schwenke (1997), Schwenke (1998); A01: Allard et al. (2001); A05: Asplund et al. (2005); B02: Burrows et al. (2002); B06: Bernath (2006); B10: T. Barman (2010, private communication); BH05: Brott & Hauschildt (2005); BT06: Barber et al. (2006); D03: Dulick et al. (2003); DA99: Davis & Allard (1999, private communication); F99: R. D. Freedman (1999, private communication); GN93: Grevesse & Noels (1993); PD93: Phillips & Davis (1993); W09: Witte et al. (2009).

Table 6. Best-fit Atmospheric Models

Spectral range	PHOENIX-Gaia		Ames-Dusty		Gaia-Dusty		Drift-PHOENIX	
	T_{eff} (K)	$\log(g)$	T_{eff} (K)	$\log(g)$	T_{eff} (K)	$\log(g)$	T_{eff} (K)	$\log(g)$
LP 349-25								
NIR (0.95–2.42 μm)^a	2800	4.5	2800	5.5	2800	5.0	2800	5.5
All (0.81–2.42 μm)	2600	4.0	2600	4.0 ^b	2600	4.0	2600	4.0
Y (0.95–1.12 μm)	2800	4.5	2800	5.5	2800	4.5	2700	5.0
J (1.10–1.34 μm)	2900	5.5 ^b	2900	5.5	2900	5.5	2800	5.5
H (1.40–1.80 μm)	2900	5.5 ^b	2900	5.5	2900	5.5	2800	6.0 ^b
K (1.90–2.40 μm)	3000	5.5 ^b	3000	5.5	2900	5.5	2900	6.0 ^b
LHS 1901								
NIR (0.95–2.42 μm)^a	3000	5.0	3000	5.0	3000	5.0	3000	5.0
All (0.81–2.42 μm)	2900	4.5	2900	4.0 ^b	2900	4.5	2900	5.0
Y (0.95–1.12 μm)	3100	4.5	3000	5.0	3000	4.5	3000	5.0
J (1.10–1.34 μm)	3000	5.5 ^b	3000	5.5	3000	5.5	3000	5.5
H (1.40–1.80 μm)	3000	5.5 ^b	3000	5.5	3000	5.5	3000	6.0 ^b
K (1.90–2.40 μm)	3100	5.5 ^b	3100	5.5	3100	5.5	3000	5.5
G1 569B								
NIR (0.95–2.42 μm)^a	2800	4.5	2800	5.5	2800	5.0	2800	5.5^c
All (0.81–2.42 μm)	2700	4.5	2800	5.5	2700	5.0	2700	5.0 ^c
Y (0.95–1.12 μm)	2900	5.0	2900	6.0 ^b	2800	5.0	2700	5.5
J (1.10–1.34 μm)	2800	5.5 ^b	2700	5.5	2700	5.5	2700	5.5
H (1.40–1.80 μm)	2900	5.5 ^b	2800	6.0 ^b	2800	6.0 ^b	2800	6.0 ^b
K (1.90–2.40 μm)	2900	5.5 ^b	2900	5.5	2800	5.5	2800	6.0 ^b
2MASS J2206–2047								
NIR (0.95–2.42 μm)^a	2900	5.0^c	2900	6.0^b	2900	5.5	2900	5.5
All (0.81–2.42 μm)	2800	4.5	2800	6.0 ^b	2700	5.0	2800	5.5
Y (0.95–1.12 μm)	2900	5.0	2900	6.0 ^b	2800	5.0	2700	5.5
J (1.10–1.34 μm)	2900	5.5 ^b	2800	5.5	2800	5.5	3000	6.0 ^b
H (1.40–1.80 μm)	2900	5.5 ^b	2900	6.0 ^b	2900	5.5	2900	6.0 ^b
K (1.90–2.40 μm)	3000	5.5 ^b	3000	5.5	2900	5.5	2900	6.0 ^b

^aThe NIR results are our preferred choice for model atmosphere fitting, as discussed in Section 3.4.

^bThe best-fit value is at the edge of the model grid.

^cIn these rare cases ($\approx 3\%$ of all the tabulated results), a significant χ^2 minimum developed that was very discrepant from the prevailing best-fit models at ≈ 2700 – 2900 K. Thus, we selected the second best fitting model rather than: 2000 K/6.0 for G1 569B Drift-PHOENIX; 3300 K/3.5 for 2MASS J2206–2047 PHOENIX-Gaia.

Table 7. Evolutionary Model-derived Properties of LP 349-25AB

Property	Median	68.3% c.l.	95.4% c.l.
Tucson models (Burrows et al. 1997)			
LP 349-25AB system			
Age (Gyr)	0.141	–0.019, 0.023	–0.04, 0.05
q (M_B/M_A)	0.863	–0.019, 0.013	–0.04, 0.03
ΔT_{eff} (K)	137	–15, 21	–40, 50
LP 349-25A			
M_A (M_\odot)	0.065	–0.004, 0.004	–0.008, 0.008
$T_{\text{eff,A}}$ (K)	2780	–30, 30	–50, 50
$\log(g_A)$ (cgs)	5.02	–0.04, 0.04	–0.08, 0.08
R_A (R_\odot)	0.130	–0.003, 0.003	–0.005, 0.006
$\text{Li}_A/\text{Li}_0^{\text{a}}$	0.75	–0.52, 0.15	–0.74, 0.22
LP 349-25B			
M_B (M_\odot)	0.056	–0.003, 0.004	–0.006, 0.007
$T_{\text{eff,B}}$ (K)	2640	–30, 30	–60, 60
$\log(g_B)$ (cgs)	5.00	–0.04, 0.04	–0.08, 0.08
R_B (R_\odot)	0.124	–0.003, 0.003	–0.005, 0.005
$\text{Li}_B/\text{Li}_0^{\text{a}}$	0.96	–0.08, 0.03	–0.28, 0.04
Lyon models (Dusty; Chabrier et al. 2000)			
LP 349-25AB system			
Age (Gyr) ^a	0.127	–0.017, 0.021	–0.03, 0.04
q (M_B/M_A)	0.872	–0.018, 0.014	–0.04, 0.03
ΔT_{eff} (K)	134	–15, 20	–40, 50
LP 349-25A			
M_A (M_\odot)	0.064	–0.004, 0.005	–0.007, 0.009
$T_{\text{eff,A}}$ (K)	2660	–30, 30	–50, 50
$\log(g_A)$ (cgs)	4.93	–0.04, 0.04	–0.08, 0.09
R_A (R_\odot)	0.144	–0.003, 0.003	–0.006, 0.006
$\text{Li}_A/\text{Li}_0^{\text{a}}$	0.68	–0.42, 0.24	–0.64, 0.30
$(J - K)_A$ (mag)	0.795	–0.002, 0.002	–0.003, 0.004
$(H - K)_A$ (mag)	0.375	–0.006, 0.005	–0.011, 0.011
$(J - H)_A$ (mag)	0.420	–0.005, 0.004	–0.008, 0.008
$(K - L')_A$ (mag)	0.544	–0.009, 0.008	–0.017, 0.016
LP 349-25B			
M_B (M_\odot)	0.056	–0.004, 0.004	–0.007, 0.007
$T_{\text{eff,B}}$ (K)	2520	–30, 30	–60, 60
$\log(g_B)$ (cgs)	4.91	–0.04, 0.04	–0.08, 0.08
R_B (R_\odot)	0.137	–0.003, 0.003	–0.005, 0.006
$\text{Li}_B/\text{Li}_0^{\text{a}}$	0.95	–0.18, 0.04	–0.54, 0.05
$(J - K)_B$ (mag)	0.810	–0.005, 0.006	–0.008, 0.013
$(H - K)_B$ (mag)	0.396	–0.009, 0.006	–0.013, 0.013
$(J - H)_B$ (mag)	0.415	–0.004, 0.005	–0.007, 0.007
$(K - L')_B$ (mag)	0.594	–0.011, 0.012	–0.021, 0.025

^aAbundance of lithium relative to the initial amount (Li_0).

Table 8. Evolutionary Model-derived Properties of LHS 1901AB

Property	Median	68.3% c.l.	95.4% c.l.
Tucson models (Burrows et al. 1997)			
LHS 1901AB system			
Age (Gyr) ^a	0.37	–0.15, 9.63	–0.21, 9.63
q (M_B/M_A)	0.966	–0.016, 0.011	–0.04, 0.02
ΔT_{eff} (K)	35	–8, 10	–24, 32
LHS 1901A			
M_A (M_\odot)	0.098	–0.010, 0.004	–0.018, 0.008
$T_{\text{eff,A}}$ (K)	2960	–30, 30	–70, 60
$\log(g_A)$ (cgs)	5.22	–0.07, 0.03	–0.14, 0.04
R_A (R_\odot)	0.128	–0.004, 0.004	–0.007, 0.009
LHS 1901B			
M_B (M_\odot)	0.095	–0.011, 0.005	–0.019, 0.007
$T_{\text{eff,B}}$ (K)	2930	–40, 30	–80, 60
$\log(g_B)$ (cgs)	5.23	–0.08, 0.03	–0.15, 0.04
R_B (R_\odot)	0.124	–0.003, 0.004	–0.006, 0.010
Lyon models (Dusty; Chabrier et al. 2000)			
LHS 1901AB system			
Age (Gyr) ^a	0.28	–0.08, 9.72	–0.13, 9.72
q (M_B/M_A)	0.958	–0.014, 0.015	–0.04, 0.03
ΔT_{eff} (K)	39	–9, 10	–27, 35
LHS 1901A			
M_A (M_\odot)	0.099	–0.011, 0.008	–0.020, 0.013
$T_{\text{eff,A}}$ (K)	2860	–50, 50	–90, 80
$\log(g_A)$ (cgs)	5.15	–0.07, 0.07	–0.15, 0.08
R_A (R_\odot)	0.138	–0.005, 0.006	–0.008, 0.012
$(J - K)_A$ (mag)	0.787	–0.001, 0.001	–0.002, 0.002
$(H - K)_A$ (mag)	0.336	–0.009, 0.009	–0.013, 0.018
$(J - H)_A$ (mag)	0.451	–0.009, 0.008	–0.017, 0.010
LHS 1901B			
M_B (M_\odot)	0.094	–0.010, 0.010	–0.019, 0.014
$T_{\text{eff,B}}$ (K)	2820	–40, 50	–90, 90
$\log(g_B)$ (cgs)	5.15	–0.07, 0.08	–0.15, 0.09
R_B (R_\odot)	0.135	–0.005, 0.006	–0.008, 0.012
$(J - K)_B$ (mag)	0.788	–0.001, 0.001	–0.002, 0.002
$(H - K)_B$ (mag)	0.341	–0.010, 0.009	–0.014, 0.019
$(J - H)_B$ (mag)	0.447	–0.008, 0.009	–0.016, 0.012

^aBoth sets of evolutionary models are only computed up to an age of 10 Gyr; therefore, this defines the upper limit on the model-derived ages.

Table 9. Evolutionary Model-derived Properties of Gl 569Bab

Property	Median	68.3% c.l.	95.4% c.l.
Tucson models (Burrows et al. 1997)			
Gl 569Bab system			
Age (Gyr)	0.51	−0.08, 0.13	−0.14, 0.38
q ($M_{\text{Bb}}/M_{\text{Ba}}$)	0.886	−0.017, 0.021	−0.03, 0.05
ΔT_{eff} (K)	229	−19, 19	−37, 39
Gl 569Ba			
M_{Ba} (M_{\odot})	0.074	−0.004, 0.004	−0.007, 0.007
$T_{\text{eff,Ba}}$ (K)	2530	−30, 30	−50, 50
$\log(g_{\text{Ba}})$ (cgs)	5.30	−0.04, 0.03	−0.07, 0.06
R_{Ba} (R_{\odot})	0.101	−0.002, 0.002	−0.003, 0.003
$\text{Li}_{\text{Ba}}/\text{Li}_0^{\text{a}}$	0.00	−0.00, 0.00	−0.00, 0.00
Gl 569Bb			
M_{Bb} (M_{\odot})	0.066	−0.004, 0.005	−0.008, 0.010
$T_{\text{eff,Bb}}$ (K)	2300	−30, 30	−60, 60
$\log(g_{\text{Bb}})$ (cgs)	5.28	−0.05, 0.05	−0.09, 0.10
R_{Bb} (R_{\odot})	0.097	−0.002, 0.002	−0.004, 0.004
$\text{Li}_{\text{Bb}}/\text{Li}_0^{\text{a}}$	0.02	−0.02, 0.49	−0.02, 0.82
Lyon models (Dusty; Chabrier et al. 2000)			
Gl 569Bab system			
Age (Gyr)	0.46	−0.07, 0.11	−0.13, 0.33
q ($M_{\text{Bb}}/M_{\text{Ba}}$)	0.866	−0.014, 0.019	−0.03, 0.05
ΔT_{eff} (K)	221	−18, 19	−36, 38
Gl 569Ba			
M_{Ba} (M_{\odot})	0.075	−0.004, 0.004	−0.008, 0.008
$T_{\text{eff,Ba}}$ (K)	2430	−30, 30	−50, 50
$\log(g_{\text{Ba}})$ (cgs)	5.23	−0.04, 0.04	−0.08, 0.06
R_{Ba} (R_{\odot})	0.110	−0.002, 0.002	−0.003, 0.005
$\text{Li}_{\text{Ba}}/\text{Li}_0^{\text{a}}$	0.00	−0.00, 0.00	−0.00, 0.00
$(J - K)_{\text{Ba}}$ (mag)	0.827	−0.007, 0.010	−0.013, 0.021
$(H - K)_{\text{Ba}}$ (mag)	0.371	−0.005, 0.007	−0.009, 0.018
$(J - H)_{\text{Ba}}$ (mag)	0.456	−0.004, 0.004	−0.008, 0.009
$(K - L')_{\text{Ba}}$ (mag)	0.660	−0.014, 0.014	−0.03, 0.03
Gl 569Bb			
M_{Bb} (M_{\odot})	0.065	−0.004, 0.005	−0.008, 0.010
$T_{\text{eff,Bb}}$ (K)	2210	−30, 30	−60, 60
$\log(g_{\text{Bb}})$ (cgs)	5.20	−0.05, 0.05	−0.09, 0.11
R_{Bb} (R_{\odot})	0.106	−0.003, 0.002	−0.005, 0.004
$\text{Li}_{\text{Bb}}/\text{Li}_0^{\text{a}}$	0.00	−0.00, 0.02	−0.00, 0.43
$(J - K)_{\text{Bb}}$ (mag)	0.96	−0.03, 0.03	−0.05, 0.06
$(H - K)_{\text{Bb}}$ (mag)	0.432	−0.017, 0.014	−0.03, 0.04
$(J - H)_{\text{Bb}}$ (mag)	0.525	−0.011, 0.013	−0.02, 0.03
$(K - L')_{\text{Bb}}$ (mag)	0.786	−0.016, 0.015	−0.03, 0.03

^a Abundance of lithium relative to the initial amount (Li_0).